IMA Journal of Applied Mathematics (2015) Page 1 of 29
doi:10.1093/imamat/hxv011

Regularized model of post-touchdown configurations in electrostatic MEMS: interface dynamics

A. E. LINDSAY*
Department of Applied and Computational Mathematics and Statistics, University of Notre Dame, South Bend, IN 46556, USA
*Corresponding author: a.lindsay@nd.edu

AND

J. LEGA AND K. B. GLASNER
Department of Mathematics, University of Arizona, Tucson, AZ 85721, USA
lega@math.arizona.edu kglasner@math.arizona.edu

[Received on 3 October 2014; revised on 3 March 2015; accepted on 17 April 2015]

Interface dynamics of post-contact states in regularized models of electrostatic–elastic interactions are analysed. A canonical setting for our investigations is the field of Micro-Electromechanical Systems (MEMS) in which flexible elastic structures may come into physical contact due to applied Coulomb forces. We study the dynamic features of a recently derived regularized model (Lindsay, A. E. *et al.* 2014 Regularized model of post-touchdown configurations in electrostatic MEMS: equilibrium analysis. *Physica D*), which describes the system beyond the quenching singularity associated with touchdown, that is after the components of the device have come together. We build on our previous investigations of steady-state solutions by describing how the system relaxes towards these equilibria. This is accomplished by deriving a reduced dynamical system that governs the evolution of the contact set, thereby providing a detailed description of the intermediary dynamics associated with this bistable system. The analysis yields important practical information on the timescales of equilibration.

Keywords: singular perturbation techniques; nano-technology; interface dynamics; mechanical bistability.

1. Introduction

The combination of Coulomb interactions and elastic forces is responsible for complex dynamics and intricate equilibrium structures observed in many physical systems. In the applied science fields of Micro-Electromechanical Systems (MEMS) and self-assembly, these forces are delicately balanced to engineer a variety of miniaturized technologies. In situations where electrostatic forces overwhelm restorative elastic forces, an event known as *pull-in* may occur where charged electrical structures come into physical contact resulting in a divergence of the local electric potential. In canonical mathematical models of this phenomenon, pull-in is manifested by a quenching finite time singularity and a corresponding loss of solution existence (Pelesko, 2002). This highlights a deficiency in many current models in that they provide no information on the potential configurations of the system after this critical event.

A simple setting to explore this scenario arises in capacitor-type MEMS devices where an elastic membrane is held fixed along its boundary above an inelastic substrate. When an electric potential V is applied between these plates, the upper elastic surface deflects downwards towards the substrate (cf.

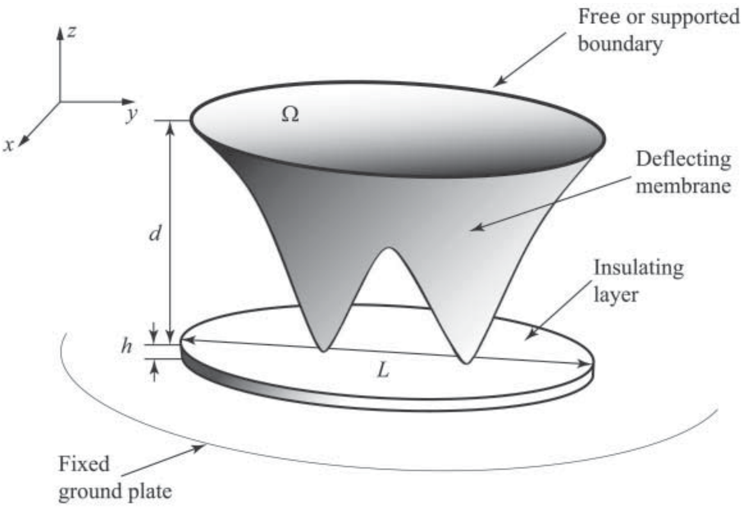

FIG. 1. Schematic diagram of a MEMS capacitor with an insulating layer of thickness h. The height of the structure and the length of the plate are not to scale; typically $d \ll L$. Reproduced from Lindsay *et al.* (2014).

Fig. 1). If V is large enough, the deflecting top plate will *touch down* on the substrate. In a preliminary attempt to characterize the dynamics of the system after initial contact between the elastic surface and the substrate, regularizing terms were derived in Lindsay *et al.* (2014). These results augment commonly studied models in the literature (Pelesko & Bernstein, 2002) and account for a variety of physical effects that take place when the gap spacing shrinks to zero. As described in Lindsay *et al.* (2014), the new model for the dimensionless deflection $u(x,t)$ of the upper membrane reads

$$\frac{\partial u}{\partial t} = -\beta\Delta^2 u + \Delta u - \frac{\lambda}{(1+u)^2} + \frac{\lambda\varepsilon^{m-2}}{(1+u)^m}, \quad x \in \Omega; \qquad u = \partial_n u = 0, \quad x \in \partial\Omega,$$

for bounded regions $\Omega \subset \mathbb{R}^n$ with $n = 1, 2$ and $m > 2$. In the above equation, the parameter β describes the relative strength of flexural to tensile properties of the plate. This model is subsequently considered in two separate cases: the second-order problem,

$$\frac{\partial u}{\partial t} = \Delta u - \frac{\lambda}{(1+u)^2} + \frac{\lambda\varepsilon^{m-2}}{(1+u)^m}, \quad x \in \Omega; \qquad u = 0, \quad x \in \partial\Omega, \tag{1.1a}$$

and its fourth-order (bi-Laplacian) counterpart

$$\frac{\partial u}{\partial t} = -\Delta^2 u - \frac{\lambda}{(1+u)^2} + \frac{\lambda\varepsilon^{m-2}}{(1+u)^m}, \quad x \in \Omega; \qquad u = \partial_n u = 0, \quad x \in \partial\Omega. \tag{1.1b}$$

These two cases represent the limits of small and large β in (1.1), respectively. The non-negative parameter λ reflects the relative importance of electrostatic and elastic forces on the system. The regularizing term $\phi_m(u;\varepsilon) = \varepsilon^{m-2}(1+u)^{-m}$ was derived in Lindsay *et al.* (2014) to mimic the presence of a small insulating layer on top of the substrate which physically prevents a short circuit at touchdown. This term can also account for a variety of physical effects which take place when $u \approx -1$. For example $m = 4$

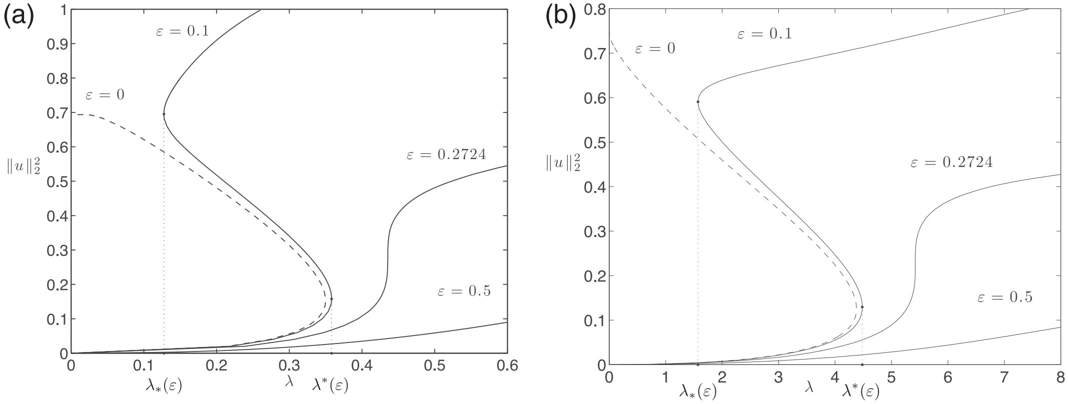

FIG. 2. Bifurcation diagrams showing equilibrium solutions of (1.1) in one dimension for $m = 4$. Left panel: Laplacian case; right panel: bi-Laplacian case. In each of the above, solution curves are plotted for $\varepsilon < \varepsilon_c$, $\varepsilon \approx \varepsilon_c$ and $\varepsilon > \varepsilon_c$ to highlight the threshold of bistability. When $\varepsilon = 0$, only two branches of solutions exist (dashed curves). Reproduced from Lindsay *et al.* (2014).

accounts for the Casimir effect while $m = 3$ models Van der Waals forces (Guo & Zhao, 2004; Batra *et al.*, 2008; Lai, 2015).

In the canonical $\varepsilon = 0$ case, the second-order formulation (1.1a) models the deformable surface as a membrane and has been featured more heavily in mathematical studies of MEMS (Pelesko, 2002; Pelesko & Bernstein, 2002; Guo *et al.*, 2005; Flores *et al.*, 2007; Guo & Wei, 2008; Brubaker & Pelesko, 2011; Kavallaris *et al.*, 2011; Brubaker & Lindsay, 2013; Kohlmann, 2013), while the fourth-order equation (1.1b), prevalent in engineering studies of MEMS as a beam description, gives much better quantitative agreement with experiments (Younis & Nayfeh, 2003; Batra *et al.*, 2007). The fourth-order system (1.1b) has recently attracted more mathematical attention as it exhibits many interesting oscillatory solution behaviours and presents significant analytical challenge due to the absence of a maximum principle (Lin & Yang, 2007; Guo & Wei, 2009; Guo, 2010; Lindsay & Ward, 2011; Lindsay & Lega, 2012; Lindsay *et al.*, 2013; Laurençot & Walker, 2014a; Lindsay, 2014).

In contrast to the standard $\varepsilon = 0$ equations, it was shown in Lindsay *et al.* (2014) that the new models (1.1) are globally well-posed and for suitable initial data satisfy $u(x,t) > -1$ for all $t > 0$. Moreover, the variational structure associated with equations (1.1) implies that their solutions will evolve to an energy minimizing equilibrium state as $t \to \infty$ if possible. As a consequence, the bifurcation diagrams of solutions to (1.1) established in Lindsay *et al.* (2014) and displayed in Fig. 2 show a new branch of equilibrium solutions (top branch of solid curves) not present in the $\varepsilon = 0$ case (dashed curve). It has large L^2-norm and appears at the fold point $\lambda = \lambda_*(\varepsilon)$ for small, positive values of ε. These minimizing solutions were explicitly constructed in Lindsay *et al.* (2014) by means of a detailed singular perturbation analysis which required systematic use of *logarithmic switchback terms*. Our analysis revealed that the new solution branch present for $\varepsilon > 0$, consists of a uniform central region where the membrane and substrate are in contact, coupled to a sharp transition layer at the boundary. The detailed scaling properties of these solutions and expressions for the extent of the contact region were established in the limit $\varepsilon \to 0$.

A notable conclusion of the analysis presented in Lindsay *et al.* (2014) is therefore that the regularized problems (1.1) are bistable over a range of ε values of the form $0 \leqslant \varepsilon \leqslant \varepsilon_c$. Bistability—the presence of two stable equilibrium states—allows for extended functionality in MEMS and is thus of great interest to practitioners (Krylov *et al.*, 2008, 2011). For example, the device may transition from

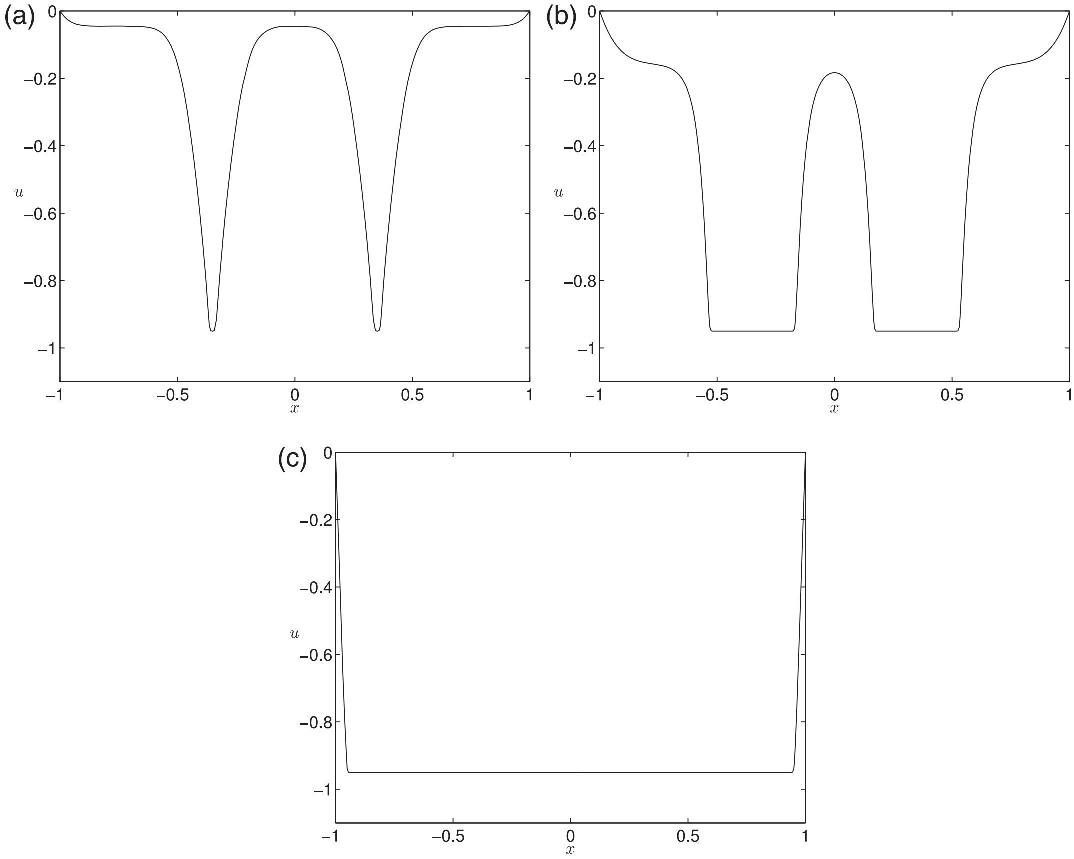

FIG. 3. Solutions of (1.1a) in one dimension with $\varepsilon = 0.05$, $\lambda = 20$ and $m = 4$. The left panel shows two initial touchdown events at $x = \pm 0.35$. The centre panel shows the growing of the contact regions and the right panel shows the equilibrium state reached after the interior fronts have merged and the outermost fronts are pinned at the boundary.

a small norm state to a large norm state over a fixed range of λ, therefore exhibiting robust switching behaviour. Bistability can also confer significant power-saving advantages to MEMS as the device can now be idled or operated near the second fold point λ_*, which occurs at a much lower value of λ and consequently lower voltage V.

This paper builds on the equilibrium analysis of Lindsay *et al.* (2014) by providing detailed quantitative descriptions of the intermediary dynamics linking the initial contact event with the new equilibrium states of equations (1.1). As many mathematical tools are geared towards understanding the behaviour of systems close to their equilibria, a major strength of this work is that we obtain detailed descriptions of the dynamics in regimes far from equilibrium, and particularly for non-radially symmetric settings in two spatial dimensions.

In the 1D setting, the typical solution behaviour considered in the present work is displayed in the numerical simulations of Fig. 3. After initial contact at one or more points, sharp interfaces form and propagate, thereafter partitioning the domain into regions of two types—a contact set where the substrate and the membrane remain together and two or more regions where they are apart. As the extent of the

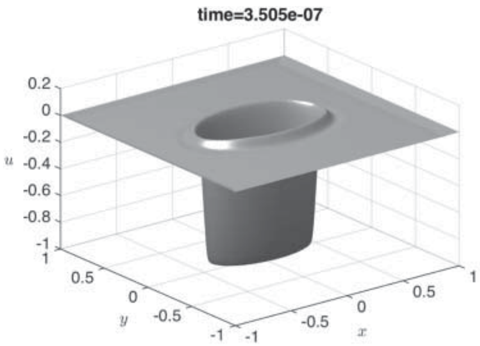

FIG. 4. Evolution of solution to (1.1b) with an initially elliptic interface. Parameter values are $\varepsilon = 0.05$, $\lambda = 8 \times 10^4$ and $m = 4$.

contact set increases, the fronts separating regions of different type either coalesce or eventually become pinned near the boundary.

In Section 2, we analyse this dynamical process with a series of detailed singular perturbation calculations of (1.1) in the limit as $\varepsilon \to 0$. This analysis leads to reduced ordinary differential equation (ODE) that show the motion of the interfaces to be driven by the local jump in the electric potential between the contact and non-contact regions. An additional analysis then describes how the spreading touchdown region slows down as it approaches the boundary of the system and settles to one of the equilibrium states described in Lindsay *et al.* (2014) (cf. Fig. 3(c)). The calculations are non-trivial on account of a multiple subscaling structure present in the vicinity of the interface which must be resolved for each subscaling before the corresponding solutions in each region can be matched together. This complexity is akin to the *triple deck* phenomenon seen in high Reynold's number flow past streamlined bodies (Stewartson & Williams, 1969) and in the dynamics of water droplets on thin films (Glasner, 2003; Glasner & Witelski, 2003).

In two spatial dimensions, the situation is more delicate as the interface between the touchdown and non-touchdown regions of the device is not point like, but often consists of closed curves in the domain. In this case, we derive in Section 3 geometric evolution laws that describe how the motion of the interface is governed by a combination of the jump in the electric potential encountered in the 1D case, and of the local curvature of the interface. In the fourth-order case (1.1b), we observe and analytically characterize non-monotone behaviour in the form of an oscillatory interface profile (cf. Fig. 4) where the amplitude of the overshoot is modulated by the curvature of the interface. From a qualitative point of view, however, the structure of 2D solutions along vertical cross sections is similar to what is observed in one space dimension.

Numerical simulations of the full equations (1.1) confirm the validity of our reduced analytical descriptions. In one spatial dimension, we implement the r-adaptive moving mesh method MOVCOL4 (cf. Russell *et al.*, 2007; Huang & Russell, 1996) to accurately track and resolve interfaces appearing in (1.1). In the 2D setting, we use a finite element method (cf. Appendix A of Lindsay *et al.*, 2013) to simulate (1.1) and the level set method (Smereka, 2003) to evolve the reduced geometric evolution laws which arise from the asymptotic reductions.

2. Interface dynamics in one dimension

In this section, the evolution of the contact points denoting the extent of the spreading touchdown region are analysed. Assuming a symmetric solution about the origin with initial contact at $x = 0$, we

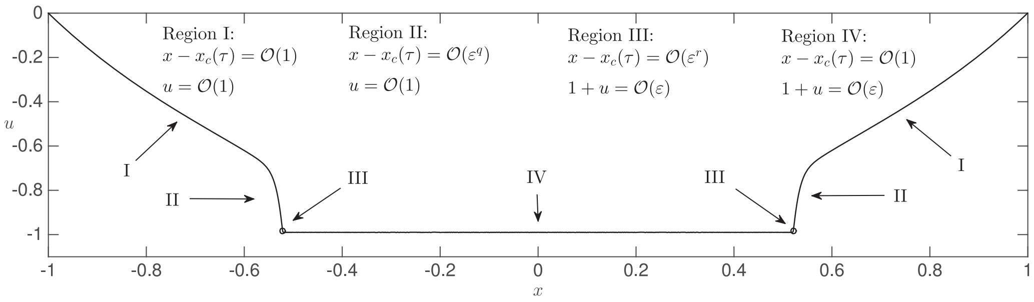

FIG. 5. Schematic diagram of typical 1D far-from-equilibrium solutions of (1.1) following a single point touchdown event. The solution consists of several layers to be resolved on a timescale $\tau = t/\varepsilon^p$. The values of the scaling parameters p, q, r are determined in the matched asymptotic analysis, and provided in (2.1) for the separate cases of (1.1a) and (1.1b).

can expect two interfaces at $x = \pm x_c(t)$. There are two cases which require separate attention. The first is when the interfaces are far from the boundary and $\pm(1 - x_c) = \mathcal{O}(1)$; second, when the interfaces begin to interact with the boundary and $\pm(1 - x_c) \ll 1$. In the former case, the structure of the solutions is displayed in Fig. 5. In the latter case, the moving contact point is pinned by the interaction with the boundaries $x = \pm 1$.

The analysis is complicated by the fact that the boundary layer ahead of the propagating interface has several sub-scales in which the solution must be resolved. The structures of the various internal layers, labelled I, II, III, IV are shown in Fig. 5. The parameters p, q and r represent the timescale of interface motion ε^p, as well as the extent of the two intermediate regions: ε^q for region II and ε^r for region III. The scaling parameters which complete the description of theses layers are found through the asymptotic analysis to be

$$\begin{aligned} &(\text{Laplacian}): \quad p = \frac{1}{2}, \quad q = \frac{1}{2}, \quad r = \frac{3}{2}; \\ &(\text{Bi-Laplacian}): \quad p = \frac{3}{4}, \quad q = \frac{1}{4}, \quad r = \frac{3}{4}. \end{aligned} \tag{2.1}$$

The structure near the boundary, in particular the shelf observed in Figs 3 and 4, or the almost linear behaviour shown in Region I of Fig. 5, is described by the leading order of the outer solution, u_0. Although the outer solution evolves over time as seen in Figs 3 and 4, the speed of the interface is estimated over shorter time scales. As a consequence, the dynamics of the interface, $\mathrm{d}x_c/\mathrm{d}t$, only depends on the value of the outer solution at the contact point, $x_c(t)$, as will be seen from Equations (2.12b) and (2.33). In order to illustrate the validity of the asymptotic expansions discussed in this section, we will select initial conditions such that the slowly evolving (relative to the speed of the interface) solution u_0 may be estimated analytically. However, the expressions for $\mathrm{d}x_c/\mathrm{d}t$ given in (2.12b) and (2.33) are established locally and therefore also apply to more general situations, and in particular when the solution on $[-1, 1]$ is not symmetric—assuming of course that an expression for $u_0(x)$ is available.

Below, we consider problems (1.1a) and (1.1b) separately, since the second-order problem is often discussed in the applied mathematics literature, whereas the fourth-order problem is more of interest to engineers.

2.1 *Laplacian case*

The cases where $\pm(1-x_c)=\mathcal{O}(1)$ and $\pm(1-x_c)\ll 1$ are treated separately in the two following subsections. In both cases, we take the definition that the moving contact point lies at the maximum of curvature, i.e. for any contact point $x_c(t)$, we have that $u_{xx}(x_c(t))=\max_{x\in\Omega} u_{xx}(x)$.

2.1.1 *Case:* $\pm(1-x_c)=\mathcal{O}(1)$

$$u_t = u_{xx} - \frac{\lambda}{(1+u)^2} + \frac{\lambda\varepsilon^{m-2}}{(1+u)^m}, \quad u\geqslant -1, \quad u(\pm 1)=0; \tag{2.2}$$

where $x_c(0)=\mathcal{O}(1)$ and $\tau = t/\varepsilon^p$. We now go through the steps of constructing a solution to (2.2) in the limit as $\varepsilon\to 0$. Region IV has extent $-x_c<x<x_c$ and here the solution is essentially uniform in value with $u=-1+\varepsilon+o(\varepsilon)$. In the vicinity of $x_c(\tau)$, the solution is composed of two boundary layers (cf. Region II and Region III in Fig. 5). For the innermost layer, Region III, the variables

$$y=\frac{x-x_c(\tau)}{\varepsilon^{3/2}}, \quad u=-1+\varepsilon v(y,t) \tag{2.3}$$

are introduced. Solutions of the resulting equations are sought via the expansion $v\sim v_0(y)+\varepsilon^{3/2-p}v_1(y)+\cdots$ and the equations for v_0 are

$$v_{0yy}=\frac{\lambda}{v_0^2}-\frac{\lambda}{v_0^m}, \quad y\in\mathbb{R}; \quad v_0(0)=\left(\frac{m}{2}\right)^{1/(m-2)}, \tag{2.4a}$$

$$v_0 = 1+\mathcal{O}(\mathrm{e}^{\sqrt{\lambda(m-2)}y}), \quad y\to-\infty; \quad v_0=\alpha y-\frac{\lambda}{\alpha^2}\log y + a_1 + \mathcal{O}\left(\frac{\log y}{y}\right), \quad y\to\infty; \tag{2.4b}$$

where the condition at $y=0$ in (2.4a) specifies that the profile is centred at the maximum curvature of v_0, i.e. $v_0(0)=\max_{y\in\mathbb{R}} v_{0yy}$. This eliminates the translation invariance of $v_0(y)$ and uniquely defines the interface location. In other words, the condition of maximum curvature at the contact point is imposed at order zero and not enforced at higher orders. The far field behaviour (2.4b) is determined by a dominant balance analysis. At the following order the problem for v_1 satisfies

$$v_{1yy}+\left[\frac{2\lambda}{v_0^3}-\frac{m\lambda}{v_0^{m+1}}\right]v_1=-v_{0y}\,\dot{x}_c, \quad y\in\mathbb{R}; \quad v_1=\mathcal{O}(y^2\,\mathrm{e}^{\sqrt{\lambda(m-2)}y}), \quad y\to-\infty; \tag{2.4c}$$

$$v_1=-\frac{\alpha\dot{x}_c}{2}\,y^2+\frac{2\lambda\dot{x}_c}{\alpha^2}\,y\log y-\frac{7\lambda\dot{x}_c}{2\alpha^2}y+\mathcal{O}(1), \quad y\to\infty, \tag{2.4d}$$

where the far behaviour (2.4d) is obtained from a particular solution to (2.4c) of form $v_{1p}=v_{0y}\int^y g(s)\mathrm{d}s$ where $g(y)$ satisfies an associated first-order equation. In the above equations, the overdot represents differentiation with respect to the fast variable τ and the parameter α is determined by multiplying (2.4a) by v_{0y} followed by integration over $\mathbb{R}$ to yield the fixed value

$$\alpha=\sqrt{\frac{2\lambda(m-2)}{m-1}}. \tag{2.5}$$

The far field behaviour generated by the solution of the system (2.4) is

$$u \sim -1 + \varepsilon \Bigg[\alpha y - \frac{\lambda}{\alpha^2}\log y + a_1 + \cdots + \varepsilon^{3/2-p}\left(-\frac{\alpha \dot{x}_c}{2} y^2 + \frac{2\lambda \dot{x}_c}{\alpha^2} y \log y - \frac{7\lambda \dot{x}_c}{2\alpha^2} y + \cdots \right)\Bigg], \quad y \to \infty. \tag{2.6}$$

If we attempt to match (2.6) to the outer solution by returning to variables (2.3) for which $y = \mathcal{O}(\varepsilon^{-3/2})$, we find the expansion is not well ordered. This indicates the presence of an intermediate layer (cf. Region II of Fig. 5) which matches with the solution valid when $x = \mathcal{O}(1)$. This intermediate asymptotic region corresponds to $y = \mathcal{O}(\varepsilon^{-1})$ and $u = \mathcal{O}(1)$ and its analysis is facilitated by introducing the variables

$$z = \frac{x - x_c(\tau)}{\varepsilon^{1/2}}, \quad u(x,t) = w(z,t), \tag{2.7}$$

which leads to the equation

$$\varepsilon w_t - \varepsilon^{1/2-p}\, w_z\, \dot{x}_c = w_{zz} - \varepsilon\lambda \left[\frac{1}{(1+w)^2} - \frac{\varepsilon^{m-2}}{(1+w)^m} \right], \quad z > 0. \tag{2.8}$$

The natural balance of terms dictates that $p = \frac{1}{2}$ and the far field behaviour of (2.6) implies that $w(z)$ has local behaviour

$$w(z) \sim -1 + \alpha z - \frac{\dot{x}_c \alpha}{2} z^2 + \cdots + \varepsilon \log\varepsilon \left[\frac{\lambda}{\alpha^2} - \frac{2\lambda \dot{x}_c}{\alpha^2} z + \cdots \right] + \varepsilon \left(a_1 - \frac{7\lambda \dot{x}_c}{2\alpha^2} z - \frac{\lambda}{\alpha^2}\log z + \frac{2\lambda \dot{x}_c}{\alpha^2} z \log z + \cdots \right), \tag{2.9}$$

as $z \to 0$. This local behaviour motivates the expansion

$$w(z) \sim w_0 + \varepsilon \log\varepsilon\, w_1 + \varepsilon w_2 + \cdots, \quad \dot{x}_c \sim \dot{x}_0 + \varepsilon \log\varepsilon\, \dot{x}_1 + \varepsilon \dot{x}_2 + \cdots,$$

and consequently a sequence of problems for w_0, w_1 and w_2 can be formulated:

$$w_{0zz} + \dot{x}_0 w_{0z} = 0, \ \ z > 0; \quad w_0(0) = -1, \ \ w_{0z}(0) = \alpha; \tag{2.10a}$$

$$w_{1zz} + \dot{x}_0 w_{1z} = -w_{0z}\dot{x}_1, \ \ z > 0; \quad w_1(0) = \frac{\lambda}{\alpha^2}, \ \ w_{1z}(0) = -\frac{2\lambda \dot{x}_0}{\alpha^2}; \tag{2.10b}$$

$$w_{2zz} + \dot{x}_0 w_{2z} = \frac{\lambda}{(1+w_0)^2} - w_{0z}\dot{x}_2, \ \ z > 0; \quad w_2 = a_1 - \frac{7\lambda \dot{x}_0}{2\alpha^2} z + \mathcal{O}(\log z), \ \ z \to 0. \tag{2.10c}$$

The exact solution of equations (2.10) is

$$w_0(z) = -1 + \frac{\alpha}{\dot{x}_0}[1 - \mathrm{e}^{-\dot{x}_0 z}], \tag{2.11a}$$

$$w_1(z) = \frac{-1}{\alpha^2 \dot{x}_0^2}[\lambda \dot{x}_0^2 + \alpha^3 \dot{x}_1 - \mathrm{e}^{-\dot{x}_0 z}(2\lambda \dot{x}_0^2 + \alpha^3 \dot{x}_1(1 + z\dot{x}_0))], \tag{2.11b}$$

$$\begin{aligned} w_2(z) = {} & \frac{\lambda}{\alpha^2}\left[\mathrm{e}^{-\dot{x}_0 z}(3 - \log[e^{\dot{x}_0 z} - 1]^2 + \log \dot{x}_0^2 + \frac{\alpha^3 \dot{x}_2}{\lambda \dot{x}_0^2}(1 + \dot{x}_0 z))\right] \\ & - \frac{\alpha}{\dot{x}_0^2}\left[\dot{x}_2 - \frac{\dot{x}_0^2}{\alpha}(a_1 - \frac{3\lambda}{\alpha^2} - \frac{\lambda}{\alpha^2}\log \dot{x}_0)\right] + \frac{\lambda}{\alpha^2}[\dot{x}_0 z + \log(1 - \mathrm{e}^{-\dot{x}_0 z})]. \end{aligned} \tag{2.11c}$$

As $z \to \infty$, the limiting behaviour of $w(z) \sim w_0 + \varepsilon \log \varepsilon\, w_1 + \varepsilon w_2 + \cdots$ has the form

$$w(z) \sim -1 + \frac{\alpha}{\dot{x}_0} - \varepsilon \log \varepsilon \left(\frac{\lambda \dot{x}_0^2 + \alpha^3 \dot{x}_1}{\alpha^2 \dot{x}_0^2}\right) - \varepsilon \left(\frac{\alpha}{\dot{x}_0^2}\left[\dot{x}_2 - \frac{\dot{x}_0^2}{\alpha}\left(a_1 - \frac{3\lambda}{\alpha^2} - \frac{\lambda}{\alpha^2}\log \dot{x}_0\right)\right] - \frac{\lambda \dot{x}_0}{\alpha^2} z\right).$$

Matching to the outer solution value $u_0(x_c)$ gives the leading-order velocity

$$\dot{x}_0 = \frac{\alpha}{1 + u_0(x_c)}, \qquad \text{where } \alpha = \sqrt{\frac{2\lambda(m-2)}{m-1}}. \tag{2.12a}$$

Since we do not expect terms in $\varepsilon \log \varepsilon$ in the outer solution, we also obtain an expression for the first-order correction $\dot{x}_1$. Moreover, if the constant (in x) component of the outer solution is independent of ε (or if $m > 3$), then matching gives the expansion for the interface velocity

$$\dot{x}_c \sim \dot{x}_0 - \frac{\dot{x}_0^2 \lambda}{\alpha^3}\varepsilon \log \varepsilon + \frac{\dot{x}_0^2}{\alpha}\left(a_1 - \frac{3\lambda}{\alpha^2} - \frac{\lambda}{\alpha^2}\log \dot{x}_0\right)\varepsilon + \cdots.$$

In returning to the original time variable $t = \tau/\varepsilon^{1/2}$ and applying (2.12a), the position of the interface x_c is thus expected to follow the three-term asymptotic ordinary differential equation

$$\frac{\mathrm{d}x_c}{\mathrm{d}t} \sim \frac{\alpha}{\varepsilon^{1/2}[1 + u_0(x_c)]} - \frac{\lambda}{\alpha}\frac{\varepsilon^{1/2}\log \varepsilon}{[1 + u_0(x_c)]^2} + \frac{\varepsilon^{1/2}}{[1 + u_0(x_c)]^2}\left[\alpha a_1 - \frac{3\lambda}{\alpha} - \frac{\lambda}{\alpha}\log \frac{\alpha}{[1 + u_0(x_c)]}\right]. \tag{2.12b}$$

The evolution law (2.12b), driven by the jump in the electric potential over the boundary layer, does not have the capacity to arrest the motion of the interface as it nears the boundary. This behaviour is expected from the variational nature of the governing equation (1.1a), the analysis of Lindsay *et al.* (2014) and observed in numerical simulations of its solution (cf. Fig. 3(c)). This motivates a separate analysis valid in the regime where the interface nears the boundary points $x = \pm 1$.

2.1.2 *Case* 2: $\pm(1 - x_c) \ll 1$. The analysis of the preceding section was based on the layer structure displayed in Fig. 5. It is reasonable to expect that the pinning region should occur once the extent of Region I has been depleted by the motion of the interface, and Region II comes into contact with the boundary, i.e. when $\pm(1 - x_c) = \mathcal{O}(\varepsilon^{1/2})$. Therefore, we consider the subinterval $x_c < x < 1$, where

$x_c = 1 - \varepsilon^{1/2}\bar{x}_c(\tau)$ and seek to solve the problem

$$u_t = u_{xx} - \frac{\lambda}{(1+u)^2} + \frac{\lambda\varepsilon^{m-2}}{(1+u)^m}, \quad u \geqslant -1, \quad u(1) = 0; \tag{2.13a}$$

$$u(1 - \varepsilon^{1/2}\bar{x}_c(\tau)) = -1 + \mathcal{O}(\varepsilon), \quad u_x(1 - \varepsilon^{1/2}\bar{x}_c(\tau)) = \mathcal{O}(\varepsilon), \tag{2.13b}$$

in the limit as $\varepsilon \to 0$. It is convenient to work with the rescaled variables

$$u(x,t) = w(z,t), \quad z = \frac{x - (1 - \varepsilon^{1/2}\bar{x}_c(\tau))}{\varepsilon^{1/2}\bar{x}_c(\tau)}, \quad \tau = \frac{t}{\varepsilon}, \tag{2.14}$$

which transform (2.13) to

$$\varepsilon\bar{x}_c^2 w_t + \dot{\bar{x}}_c\bar{x}_c[1 - z]w_z = w_{zz} - \lambda\bar{x}_c^2\varepsilon\left[\frac{1}{(1+w)^2} - \frac{\varepsilon^{m-2}}{(1+w)^m}\right], \quad 0 < z < 1; \tag{2.15a}$$

$$w(1) = 0, \quad w(0) = -1 + \mathcal{O}(\varepsilon). \tag{2.15b}$$

A leading-order solution $w = w_0 + o(1)$ is now constructed where w_0 satisfies

$$\dot{\bar{x}}_c\bar{x}_c[1 - z]w_{0z} = w_{0zz}, \quad 0 < z < 1; \quad w_0(1) = 0, \quad w_0(0) = -1, \tag{2.16a}$$

and admits the representation

$$w_0(z) = -1 + \frac{\int_0^z \exp[\dot{\bar{x}}_c\bar{x}_c(s - s^2/2)]\,\mathrm{d}s}{\int_0^1 \exp[\dot{\bar{x}}_c\bar{x}_c(s - s^2/2)]\,\mathrm{d}s}, \quad 0 < z < 1. \tag{2.16b}$$

This integral formulation generates the local behaviour

$$w_0(z) = -1 + z\left(\int_0^1 \exp[\dot{\bar{x}}_c\,\bar{x}_c(s - s^2/2)]\,\mathrm{d}s\right)^{-1} + \mathcal{O}(z^2), \quad z \to 0^+. \tag{2.17}$$

Note that $w_0'(0) \neq 0$ and therefore the zero gradient at the contact point condition must be enforced in a boundary layer centred at $z = 0$. To analyse this boundary layer, the variables

$$w(z) = -1 + \varepsilon v(y,t), \quad z = \varepsilon y \tag{2.18}$$

are employed. Seeking a leading-order solution $v \sim v_0(y) + \cdots$, we have that $v_0(y)$ satisfies

$$v_{0yy} = \lambda\bar{x}_c^2\left[\frac{1}{v_0^2} - \frac{1}{v_0^m}\right], \quad -\infty < y < \infty; \tag{2.19a}$$

$$v_0 = \alpha\bar{x}_c y + \mathcal{O}(\log y), \quad y \to \infty; \quad \alpha = \sqrt{\frac{2\lambda(m-2)}{m-1}}, \tag{2.19b}$$

$$v_0 = 1 + \mathcal{O}(\mathrm{e}^{\sqrt{\lambda(m-2)}y}), \quad y \to -\infty. \tag{2.19c}$$

The matching condition between the far field behaviours (2.19b) and the local condition (2.17) gives

$$\alpha\bar{x}_c\int_0^1 \exp[\dot{\bar{x}}_c\bar{x}_c(s-s^2/2)]\,\mathrm{d}s=1. \tag{2.20}$$

This expression is a non-linear, implicit differential equation of type $f(\bar{x}_c,\dot{\bar{x}}_c)=0$ for the evolution of the contact line. The dynamics of this system (cf. Fig. 6(a)) are characterized by the behaviour $\bar{x}_c\to 1/\alpha$ as $\tau\to\infty$ and so in terms of the original variables (2.14), the two equilibrium contact points are

$$x_c^{\pm}(\varepsilon)\sim\pm\left(1-\frac{\varepsilon^{1/2}}{\alpha}\right),\quad \text{where } \alpha=\sqrt{\frac{2\lambda(m-2)}{m-1}}. \tag{2.21}$$

The above is in agreement with Lindsay *et al.* (2014), which gives a formula for $x_c^{\pm}(\varepsilon)$ to order $\varepsilon^{3/2}$, the first terms of which are given by (2.21). The equilibrium of the dynamical system (2.20) therefore provides a good leading-order prediction of the pinned state, while the more detailed asymptotic analysis of Lindsay *et al.* (2014) yields improved accuracy over a larger range of values for ε. The squared L^2-norm of the corresponding equilibrium solutions is

$$\begin{aligned}\int_{-1}^1 u^2\,\mathrm{d}x&=2\left[\int_0^{1-\varepsilon^{1/2}\bar{x}_c}u^2\,\mathrm{d}x+\int_{1-\varepsilon^{1/2}\bar{x}_c}^1 u^2\,\mathrm{d}x+\mathcal{O}(\varepsilon^{3/2})\right]\\&=2\left[(-1+\varepsilon)^2(1-\varepsilon^{1/2}\bar{x}_c)+\varepsilon^{1/2}\bar{x}_c\int_0^1 w_0^2\,\mathrm{d}z+\mathcal{O}(\varepsilon^{3/2}\log\varepsilon)\right].\end{aligned}$$

Note that when $\dot{\bar{x}}_c=0$, $w_0(z)=-1+z$ and $\|u(x;\varepsilon)\|_2^2$ has leading-order behaviour

$$\|u\|_2^2=2\left[(-1+\varepsilon)^2\left(1-\frac{\varepsilon^{1/2}}{\alpha}\right)+\frac{1}{3}\frac{\varepsilon^{1/2}}{\alpha}+\mathcal{O}(\varepsilon^{3/2}\log\varepsilon)\right]=2\left[1-\frac{2\varepsilon^{1/2}}{3\alpha}-2\varepsilon+\mathcal{O}(\varepsilon^{3/2}\log\varepsilon)\right], \tag{2.22}$$

where α is given in (2.21). As expected, the above formula matches expression (4.11) of Lindsay *et al.* (2014).

2.1.3 *Numerical example.* In this section, we illustrate the validity of the above analysis on a numerical example. For verification of the reduced asymptotic dynamics, a ‘shelf-like’ initial condition is applied in numerical simulations of (2.2) in conjunction with parameter values $\lambda=10$, $m=4$ and $\varepsilon=0.005$. After the initial touchdown, the contact points are located by following the maxima of the second derivative of the solution. For the particular values of λ and ε, the outer solution u_0 is spatially uniform and given approximately by the solution of the ODE

$$\frac{\mathrm{d}u_0}{\mathrm{d}t}=-\frac{\lambda}{(1+u_0)^2},\quad u_0(0)=0;\ \Longrightarrow\ u_0=-1+(1-3\lambda t)^{1/3}.$$

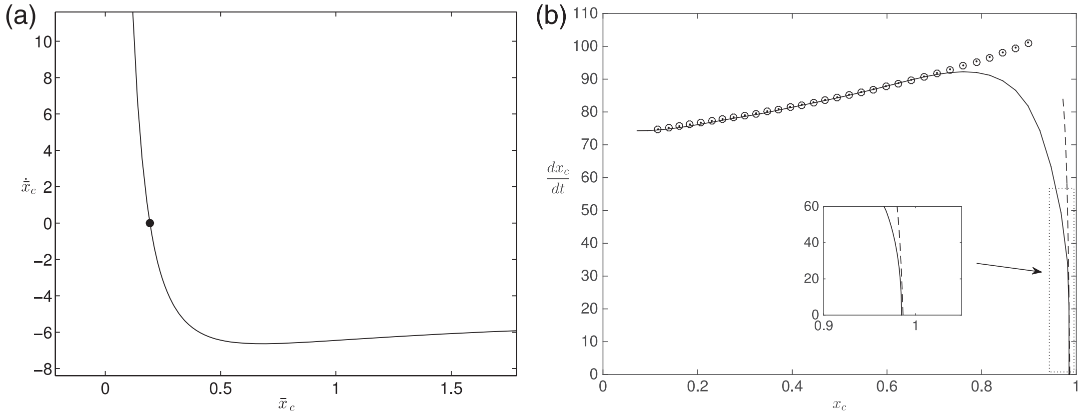

FIG. 6. The left panel displays the dynamics associated with (2.20) and $\lambda = 20$ and $m = 4$. The solid dot indicates a stable equilibrium at $\bar{x}_c = \sqrt{3/4\lambda}$. The right panel shows a comparison of the asymptotic predictions with numerical simulations (solid line) of the main equation (2.2) for $\lambda = 20$ $m = 4$ and $\varepsilon = 0.005$. The solid dots and circles represent leading-order and three-term approximations from (2.23), respectively, while the dashed line is from (2.20).

In combination with the result of (2.12b), the spreading speed of the touchdown region for this example is given, to leading order, by

$$\frac{\mathrm{d}x_c}{\mathrm{d}t} \sim \frac{\alpha}{\varepsilon^{1/2}(1-3\lambda t)^{1/3}} + \frac{\varepsilon^{1/2}}{(1-3\lambda t)^{2/3}}\left[-\frac{\lambda}{\alpha}\log\varepsilon + \alpha a_1 - \frac{3\lambda}{\alpha} - \frac{\lambda}{\alpha}\log\frac{\alpha}{(1-3\lambda t)^{1/3}}\right] \tag{2.23}$$

with $\alpha = \sqrt{4\lambda/3}$. The parameter a_1 is determined numerically from (2.4a–2.4b) and for the example case $\lambda = 20$, we calculate $a_1 = -0.577$. The accuracy of the leading-order and three-term asymptotic reductions is demonstrated in Fig. 6(b) by plotting the predictions of the interface velocities. In the regime where the interface x_c is far from the boundary, (2.23) captures the front velocity well, particularly by the leading-order term. The inclusion of the higher-order terms offers very minimal improvements to the accuracy of the asymptotic reduction. In the pinning region close to the boundary, the dynamics are accurately predicted by the implicit dynamical system (2.20).

2.2 *Bi-Laplacian problem*

2.2.1 *Front motion:* $\pm(1 - x_c(\tau)) = \mathcal{O}(1)$.

In this section, we turn to the problem of constructing the moving interface solution of the fourth-order problem

$$u_t = -u_{xxxx} - \frac{\lambda}{(1+u)^2} + \frac{\lambda\varepsilon^{m-2}}{(1+u)^m}, \quad -1 < x < 1; \quad u(\pm 1) = u_x(\pm 1) = 0 \tag{2.24}$$

together with the contact point condition $u_x(x_c(\tau)) = 0$, where $-1 < x_c(\tau) < 1$ and $\tau = t/\varepsilon^p$. The timescale for the interface is ε^p, where p will be determined. To construct a solution in the vicinity of the contact point, the variables,

$$u = -1 + \varepsilon v(y), \quad y = \frac{x - x_c(\tau)}{\varepsilon^{3/4}}, \quad \tau = \frac{t}{\varepsilon^p}, \tag{2.25}$$

are introduced into (2.24) and lead to the following problem for $v(y)$:

$$-\dot{x}_c v_y \varepsilon^{9/4-p} = -v_{yyyy} - \frac{\lambda}{v^2} + \frac{\lambda}{v^m}, \quad -\infty < y < \infty. \tag{2.26}$$

Expanding (2.26) with $v = v_0 + \varepsilon^{9/4-p} v_1 + \cdots$ gives to leading order

$$-v_{0yyyy} - \frac{\lambda}{v_0^2} + \frac{\lambda}{v_0^m} = 0, \quad -\infty < y < \infty. \tag{2.27}$$

By multiplying equation (2.26) through by v_{0y} and integrating once, a conserved quantity can be isolated with value $\alpha^2/2$ fixed by the condition $v_0 \sim 1$ as $y \to -\infty$ so that

$$-v_{0yyy}v_{0y} + \frac{1}{2}v_{0yy}^2 + \frac{\lambda}{v_0} - \frac{\lambda}{(m-1)v_0^{m-1}} = \frac{\alpha^2}{2}, \tag{2.28}$$

where $\alpha^2 = 2\lambda(m-2)/(m-1)$ is the same factor defined previously in (2.5). Consequently a balance of terms determines the far field behaviour $v_0 \sim \alpha y^2/2 + \cdots$ and v_0 satisfies

$$-v_{0yyy}v_{0y} + \frac{1}{2}v_{0yy}^2 = \frac{\lambda(m-2)}{(m-1)} - \frac{\lambda}{v_0} + \frac{\lambda}{(m-1)v_0^{m-1}}, \quad -\infty < y < \infty; \tag{2.29a}$$

$$v_0 = 1 + \mathcal{O}(\mathrm{e}^{(\lambda(m-2))^{1/4}y}) \ \ y \to -\infty; \quad v_0 = \sqrt{\frac{\lambda(m-2)}{2(m-1)}}y^2 + \xi y + \mathcal{O}(\log y), \ \ y \to \infty, \tag{2.29b}$$

and so the far field $v = v_0 + \mathcal{O}(\varepsilon^{9/4-p})$ provides the behaviour

$$u = -1 + \varepsilon\left[\sqrt{\frac{\lambda(m-2)}{2(m-1)}}y^2 + \mathcal{O}(\varepsilon^{9/4-p})\right] \quad y \to \infty. \tag{2.30}$$

The parameter ξ in (2.29b) can be fixed by removing the scale invariance of equation (2.29a) through the normalization condition $v_0(0) = \min_{y\in\mathbb{R}} v_0(y)$. The profile $v_0(y)$ can be determined numerically by posing (2.27) as a boundary value problem on a finite interval $[-L, L]$ for L large but finite. To approximate the far field condition $v_0(y) = 1 + \mathcal{O}(\exp[(\lambda(m-2))^{1/4}y])$ as $y \to -\infty$, the boundary conditions $v_0(-L) = 1, v_{0y}(-L) = v_{0yy}(-L) = 0$ are applied. To enforce the condition that $v_{0yyy} = \mathcal{O}(y^{-3})$ as $y \to \infty$, we set $v_{0yyy}(L) = 0$. The system is then solved by the MATLAB routine `bvp4c` for $L = 25$. A portion of the profile $v_0(y)$ with the global minimum centred at $y = 0$ is shown in Fig. 7.

As in the second-order problem, an attempt to match the far field behaviour (2.30) through the original coordinates (2.25) fails because expression (2.30) is $\mathcal{O}(\varepsilon^{-1/2})$ when $y = \mathcal{O}(\varepsilon^{-3/4})$. This breakdown in the ordering of the expansion indicates the presence of an intermediate scaling when $y = \mathcal{O}(\varepsilon^{-1/2})$ or $x - x_c = \mathcal{O}(\varepsilon^{1/4})$. Consequently, the intermediate scaling quantities

$$u(x) = w(z), \quad z = \frac{x - x_c}{\varepsilon^{1/4}}, \quad y = \frac{z}{\varepsilon^{1/2}},$$

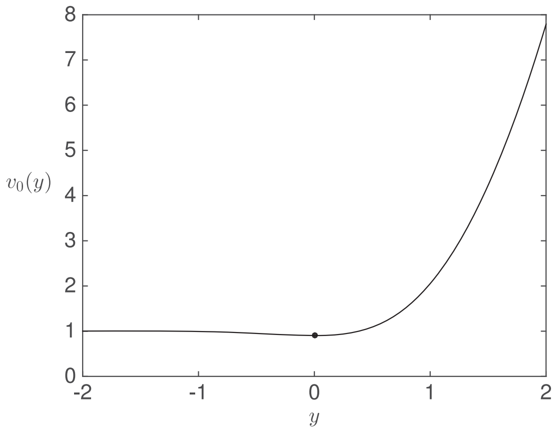

FIG. 7. The numerical solution $v_0(y)$ of the inner problem (2.29) for $m=4$ and $\lambda=27$. The solid dot is the global minimum of $v_0(y)$ with value $\min_{y\in\mathbb{R}} v_0(y) \approx 0.9033$.

are introduced which transforms (2.24) to the problem for $w(z)$,

$$\dot{x}_c w_z \varepsilon^{3/4-p} = w_{zzzz} + \varepsilon \left[\frac{\lambda}{(1+w)^2} - \frac{\varepsilon^{m-2}\lambda}{(1+w)^m} \right], \quad z > 0; \tag{2.31a}$$

$$w \sim -1 + \sqrt{\frac{\lambda(m-2)}{2(m-1)}} z^2 + \cdots, \quad z \to 0^+. \tag{2.31b}$$

The value for $p = \frac{3}{4}$ is assumed and so the expansion $w = w_0 + \cdots$ gives the leading-order problem

$$\dot{x}_c w_{0z} = w_{0zzzz}, \ \ z > 0; \quad w_0 \sim -1 + \sqrt{\frac{\lambda(m-2)}{2(m-1)}} z^2 + \cdots, \ \ z \to 0^+, \tag{2.32a}$$

whose solution is

$$w_0(z) = -1 + \frac{2}{\dot{x}_c^{2/3}} \sqrt{\frac{\lambda(m-2)}{2(m-1)}} \left[1 - \frac{2}{\sqrt{3}} \mathrm{e}^{-\dot{x}_c^{1/3}(z/2)} \cos\left(\frac{\sqrt{3}}{2} \dot{x}_c^{1/3} z - \frac{\pi}{6} \right) \right]. \tag{2.32b}$$

In the limit as $z \to \infty$, (2.32b) provides the condition

$$u_0(x_c) = -1 + \frac{2}{\dot{x}_c^{2/3}} \sqrt{\frac{\lambda(m-2)}{2(m-1)}} \quad \Longrightarrow \quad \dot{x}_c^{2/3} = \frac{2}{1+u_0(x_c)} \sqrt{\frac{\lambda(m-2)}{2(m-1)}}, \tag{2.33}$$

where $u_0(x)$ is the leading-order term of the outer solution.

2.2.2 *Pinning region*: $\pm(1-x_c) \ll 1$. In this regime, the intermediate region interacts with the boundary and acts to pin the moving front. To facilitate the analysis of this process, the rescaling

$x_c = \pm(1 - \varepsilon^{1/4}\bar{x}_c)$ and the stretched variables,

$$u(x,t) = w(z,t), \quad z = \frac{x - (1 - \varepsilon^{1/4}\bar{x}_c(\tau))}{\varepsilon^{1/4}\bar{x}_c(\tau)}, \quad \tau = \frac{t}{\varepsilon}, \tag{2.34}$$

are employed. A leading-order solution $w = w_0 + o(1)$ is sought where $w_0(z)$ satisfies

$$\begin{gathered} \dot{\bar{x}}_c \bar{x}_c^3 (1-z) w_{0z} = -w_{0zzzz}, \quad 0 < z < 1; \\ w_0(1) = 0, \quad w_{0z}(1) = 0, \quad w_0(0) = -1, \quad w_{0z}(0) = 0. \end{gathered} \tag{2.35a}$$

While equation (2.35a) does not have a convenient closed-form solution, we can proceed by observing the local behaviour

$$w_0(z) \sim -1 + \chi(\bar{x}_c, \dot{\bar{x}}_c) z^2/2 + \cdots, \quad z \to 0; \quad \chi(\bar{x}_c, \dot{\bar{x}}_c) = w_{0zz}(0), \tag{2.35b}$$

where the quantity $\chi(\bar{x}_c, \dot{\bar{x}}_c)$ will be matched to a local solution near the interface. In the vicinity of $z = 0$, a local solution of form $w = -1 + \varepsilon v(y)$, $z = \varepsilon^{1/2} y$ is developed. At leading order the problem for $v(y)$, with growth as $y \to \infty$ prescribed by (2.35b), is

$$-v_{yyyy} = \frac{\lambda \bar{x}_c^4}{v^2} - \frac{\lambda \bar{x}_c^4}{v^m}, \quad \infty < y < \infty; \tag{2.36a}$$

$$v = 1 + \mathcal{O}(\mathrm{e}^{(\lambda(m-2))^{1/4}\bar{x}_c y}), \ \ y \to -\infty; \quad v = \chi(\bar{x}_c, \dot{\bar{x}}_c)\frac{y^2}{2} + \mathcal{O}(\log y), \ \ y \to \infty. \tag{2.36b}$$

The standard solvability techniques now give the condition

$$\chi^2(\bar{x}_c, \dot{\bar{x}}_c) = \frac{2\lambda(m-2)\bar{x}_c^4}{m-1}, \tag{2.37}$$

which constitutes an implicit ODE for $\bar{x}_c(\tau)$. If initial conditions are specified, $w_{0zz}(0) = \chi(\bar{x}_c, \dot{\bar{x}}_c)$ can be evaluated numerically, and (2.37) leads to relationship between $\bar{x}_c$ and $\dot{\bar{x}}_c$. For the example discussed in Section 2.2.3, a graph of $\dot{\bar{x}}_c$ as a function of $\bar{x}_c$ is shown in Fig. 9 for $\lambda = 4 \times 10^5$ and $m = 4$. As $\dot{\bar{x}}_c \to 0$, $\chi(\bar{x}_c, \dot{\bar{x}}_c) \to 6$ which in turn gives the dynamics $\bar{x}_c \to (18(m-1)/\lambda(m-2))^{1/4}$ as $\tau \to \infty$. A leading-order prediction for the two contact points is thus given to be

$$x_c^{\pm}(\varepsilon) = \pm\left(1 - \left[\frac{18\varepsilon(m-1)}{\lambda(m-2)}\right]^{1/4}\right). \tag{2.38}$$

The equilibrium solutions attained after the moving front pins at the boundary can also be characterized by their squared L^2-norm. The calculation follows steps similar to those leading to (2.22), and results in

$$\|u(x;\varepsilon)\|_2^2 = 2\left[1 - \frac{22}{35}\left(\frac{18(m-1)}{\lambda(m-2)}\right)^{1/4} \varepsilon^{1/4} + \mathcal{O}(\varepsilon^{3/4})\right]. \tag{2.39}$$

The results (2.38) and (2.39) agree to leading order with the more detailed analysis of Lindsay *et al.* (2014).

2.2.3 *Numerical example.* In this section, a carefully chosen example is constructed to demonstrate the qualitative and quantitative efficacy of the previous asymptotic descriptions. An issue for quantitative comparisons with the velocity (2.33) is that one needs information on the outer solution $u_0(x_c)$. To arrive at a closed-form expression for $u_0(x_c)$, one may consider a scenario whereby the computational domain is sufficiently large to allow for a touchdown region, originating at $x=0$, to evolve without interaction with the boundary. In such a scenario, the solution profile away from the boundary and the interface x_c would be largely governed by the ODE problem

$$\frac{\mathrm{d}u_0}{\mathrm{d}t} = -\frac{\lambda}{(1+u_0)^2}, \quad u_0(0)=0; \implies u_0 = -1 + (1-3\lambda t)^{1/3}. \tag{2.40}$$

A ‘sufficiently large’ computational domain, as discussed in the previous paragraph, may comprise something like $\Omega = [-L, L]$ for $L \approx 25$. For reasons of convenience, our numerical simulations are performed on the interval $\Omega = [-1, 1]$, and consequently the rescaling generates a large effective λ value which scales $\lambda \propto L^4$. Indeed, our simulations are run with $\lambda = 4 \times 10^5$ which, as seen in Fig. 3(b), generates a ‘shelf-like’ uniform interior solution corresponding to u_0 given by (2.40). A combination of the uniform interior solution (2.40) and the asymptotic velocity (2.33) gives the explicit interface velocity

$$\frac{\mathrm{d}x_c}{\mathrm{d}t} \sim \frac{1}{\sqrt{1-3\lambda t}} \left[\frac{\lambda(m-2)}{\varepsilon(m-1)}\right]^{3/4} + \cdots . \tag{2.41}$$

The combination of large and small numerical parameters, in conjunction with the presence of multiple sharp interfaces, renders accurate numerical simulation of (2.24) a non-trivial exercise. To resolve the large gradients in the system effectively, we have implemented the r-adaptive scheme MOVCOL4 (Russell *et al.*, 2007) which seeks to allocate mesh points based on equidistribution of a monitor function over each computational subinterval. The method solves an associated moving mesh PDE (MMPDE) together with the underlying equation (2.24) whose discretization results in a large system of stiff ODEs. The solution is estimated between the mesh points using a seventh-order polynomial interpolation. More details of the method are given in the Appendix of Lindsay & Lega (2012).

The numerical simulations of (2.24) are initialized with the ‘inverted top-hat’ initial condition seen in Fig. 8(a), which generates a localized touchdown event around $x=0$ shortly after initialization. The initial mesh, indicated by the crosses below the profile, is congregated around the initial interface. In the dynamical spreading of the touchdown region which follows, the multiple layers of the solution develop as seen in Fig. 8(b) and their locations are tracked by the computational mesh.

The oscillatory features of the solution in Region II (cf. Fig. 5), as predicted by the explicit solution (2.32b) in that layer, are particularly apparent in Fig. 8(b). These oscillatory features illustrate the fact that the fourth-order equation (2.24) does not preserve the sign of its initial data, in contrast to the second-order equation (2.2). As the interface nears the boundary, it decelerates and its motion is eventually arrested. From Section 2.2.2, we have the prediction that $\mathrm{d}x_c/\mathrm{d}t = -\varepsilon^{-3/4}\dot{\bar{x}}_c$ where $\dot{\bar{x}}_c$ satisfies the implicit ODE (2.37) whose dynamics is displayed in Fig. 9(a). In Fig. 9(b), the interface velocities predicted by the two asymptotic analyses are shown to agree very well with the numerical simulations.

The structure of the new stable equilibria attained in Fig. 8(c) has been analysed in significant detail in Lindsay *et al.* (2014). As in the Laplacian case, the analysis of the pinning regime in Section 2.2.2 captures the leading-order properties of this branch of solutions.

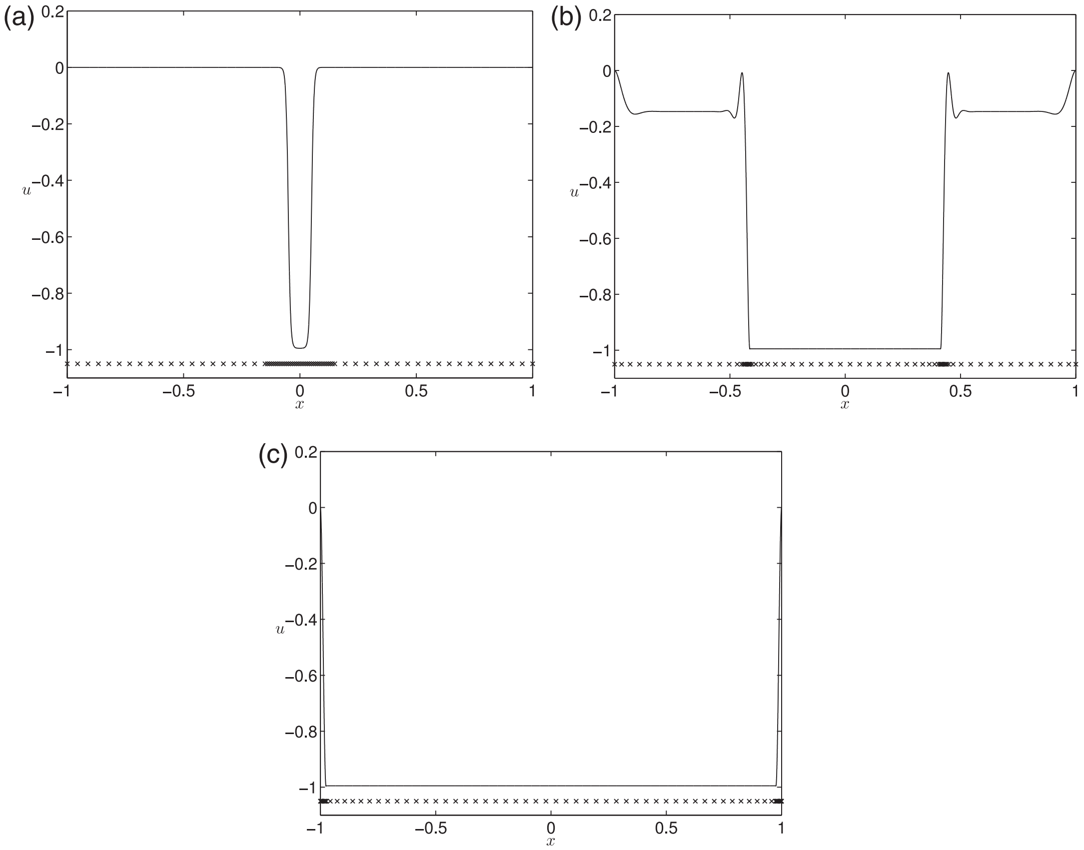

Fig. 8. Solution profiles for equation (2.24) with parameter values $m = 4$, $\lambda = 4 \times 10^5$ and $\varepsilon = 0.005$. Profiles correspond, from left to right, to solutions at increasing times. The crosses displayed below the solution curve indicate the mesh points of the discretization and are observed to aggregate around the interface and track it as it evolves. (a) Initial condition. (b) Spreading of touchdown region. (c) Boundary pinning.

3. Dynamics of contact set boundary in two dimensions

In this section, we investigate the dynamical evolution of the touchdown region in a bounded 2D region $\varOmega$. More specifically, we consider a closed a curve $\varGamma(x, t; \varepsilon) = 0$ for which $\varGamma^- = \{x \in \varOmega \mid \varGamma < 0\}$ represents the region where touchdown has already occurred, i.e. where $u \simeq -1 + \varepsilon$. On the other hand, $\varGamma^+ = \{x \in \varOmega \mid \varGamma > 0\}$ represents the region where the two surfaces are not yet in contact. In order to give a description of the interface evolution, it is helpful to utilize a fitted orthogonal system ρ, s, where ρ is the signed distance from the boundary $\varGamma = 0$, while on $\varGamma$ the coordinate s denotes the arc-length along the interface. In this coordinate system (cf. Fife, 1988; Lindsay & Glasner, 2013), the Laplacian operator and the time derivative have the representation

$$\varDelta u \equiv \frac{\partial^2 u}{\partial \rho^2} - \frac{\kappa}{1 - \kappa\rho}\frac{\partial u}{\partial \rho} + \frac{1}{1 - \kappa\rho}\frac{\partial}{\partial s}\left(\frac{1}{1 - \kappa\rho}\frac{\partial u}{\partial s}\right), \tag{3.1a}$$

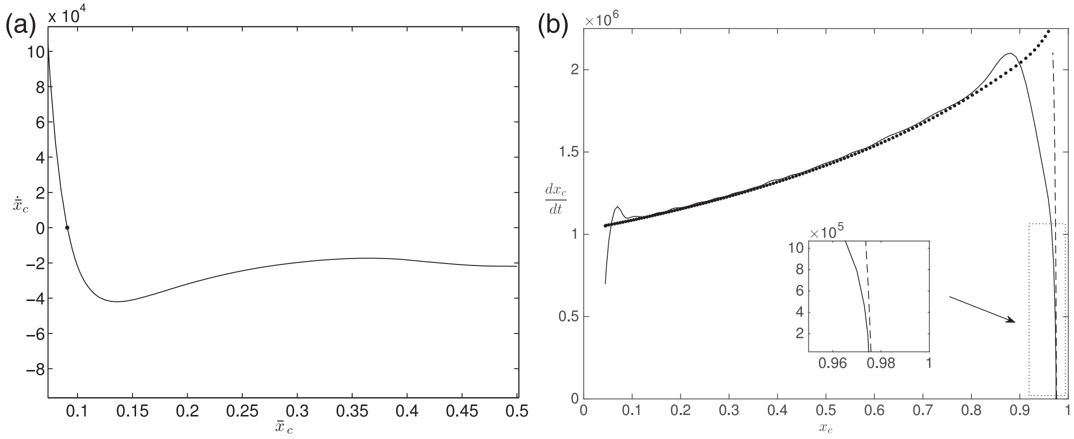

FIG. 9. The left panel shows the numerically obtained dynamics $\dot{\bar{x}}_c$ versus $\bar{x}_c$ associated with (2.37) for $\lambda = 4 \times 10^5$ and $m = 4$. The solid dot indicates the stable equilibrium $\bar{x}_c = (27/\lambda)^{1/4} \approx 0.0906$. The right panel shows a comparison of the interface velocity from full numerical simulations (solid line) of (2.24) as shown in Fig. 8. The dotted line corresponds to the asymptotic velocity (2.41), derived assuming that $\pm(1 - x_c) = \mathcal{O}(1)$, while the dashed line corresponds to the velocity derived when $\pm(1 - x_c) \ll 1$. The asymptotic prediction for the equilibrium contact point $x_c = 1 - \varepsilon^{1/4}\bar{x}_c \approx 0.9759$ is seen to be quite accurate.

$$\frac{\mathrm{d}u}{\mathrm{d}t} \equiv \frac{\partial u}{\partial t} + \rho_t \frac{\partial u}{\partial \rho} + s_t \frac{\partial u}{\partial s}, \tag{3.1b}$$

where $\kappa(s)$ is the curvature along Γ. As in the 1D case, we treat the Laplacian and bi-Laplacian cases separately.

3.1 *Laplacian case*

Here we begin by analysing the equation

$$\partial_t u + \rho_t \partial_\rho u + s_t \partial_s u = \frac{\partial^2 u}{\partial \rho^2} - \frac{\kappa}{1 - \kappa\rho} \frac{\partial u}{\partial \rho} + \frac{1}{1 - \kappa\rho} \frac{\partial}{\partial s} \left(\frac{1}{1 - \kappa\rho} \frac{\partial u}{\partial s} \right) - \frac{\lambda}{(1+u)^2} + \frac{\lambda \varepsilon^{m-2}}{(1+u)^m}, \tag{3.2}$$

by first considering the local problem in the vicinity of the interface $\Gamma(t;\varepsilon) = 0$. After balancing arguments akin to those performed for the 1D problem, one finds that the scales of the boundary layers and fast time scale of the interface are unchanged from that of the 1D problem. Hence the analysis begins by considering the equation in the corner layer with the variables

$$y = \frac{\rho(\tau, s; \varepsilon)}{\varepsilon^{3/2}}, \quad u = -1 + \varepsilon v(\rho, s, t; \varepsilon), \quad \tau = \varepsilon^{1/2} t, \tag{3.3}$$

which transforms (3.2) to

$$\varepsilon v_y \dot{\rho} = v_{yy} - \kappa \varepsilon^{3/2} v_y - \frac{\lambda}{v^2} + \frac{\lambda}{v^m} + \mathcal{O}(\varepsilon^3), \quad -\infty < y < \infty; \tag{3.4a}$$

$$v_{yy}(0) = \max_{y \in \mathbb{R}} v_{yy}, \tag{3.4b}$$

where an overdot represents differentiation with respect to τ. The second condition (3.4b) uniquely locates the interface at the maximum of the second derivative of the solution, i.e. at the point of maximum curvature along the profile. As in the 1D case, we will only enforce this condition at leading order. The quantities $\dot{\rho}$ and v in equation (3.4) are further expanded as

$$\dot{\rho} = \dot{\rho}_0 + \varepsilon^{1/2}\dot{\rho}_1 + o(\varepsilon^{1/2}), \quad v = v_0 + \varepsilon v_1 + \varepsilon^{3/2} v_2 + o(\varepsilon^{1/2}) \tag{3.5}$$

and terms gathered at various orders. The leading-order cross-sectional interface profile v_0 is that of the 1D problem (2.4) and satisfies

$$v_{0zz} = \frac{\lambda}{v_0^2} - \frac{\lambda}{v_0^m}, \quad -\infty < y < \infty; \quad v_0(0) = \left(\frac{m}{2}\right)^{1/(m-2)}; \tag{3.6a}$$

$$v_0 = 1 + \mathcal{O}(\mathrm{e}^{\sqrt{\lambda(m-2)}y}), \;\; y \to -\infty; \quad v_0 = \alpha y + \mathcal{O}(\log y), \;\; y \to \infty, \tag{3.6b}$$

where the constant α is determined to be

$$\alpha = \sqrt{\frac{2\lambda(m-2)}{m-1}}$$

by multiplying (3.6a) by v_{0z} and integrating over $\mathbb{R}$. The normalization condition on $v_0(0)$ appearing in (3.6a) replaces condition (3.4b) by noting that $v_0 > 1$ from maximum principle considerations and that $f(s) = s^2 - s^{-m}$ attains its global maximum at $s = (m/2)^{1/(m-2)}$ for $s > 1$. At the following order, the correction term v_1 is

$$v_{1zz} + \left(\frac{2\lambda}{v_0^3} - \frac{m\lambda}{v_0^m}\right) v_1 = \dot{\rho}_0 v_{0z}, \quad -\infty < y < \infty; \tag{3.7a}$$

$$v_1 = \mathcal{O}(y^2\,\mathrm{e}^{\sqrt{\lambda(m-2)}y}), \;\; y \to -\infty; \quad v_1 = \frac{\alpha\dot{\rho}_0}{2} y^2 + \mathcal{O}(y\log y), \;\; y \to \infty, \tag{3.7b}$$

while for v_2,

$$v_{2zz} + \left(\frac{2\lambda}{v_0^3} - \frac{m\lambda}{v_0^m}\right) v_2 = -(\dot{\rho}_1 + \kappa) v_{0z}, \quad -\infty < y < \infty; \tag{3.8a}$$

$$v_2 = \mathcal{O}(y^2\,\mathrm{e}^{\sqrt{\lambda(m-2)}y}), \;\; y \to -\infty; \quad v_2 = -\frac{\alpha(\dot{\rho}_1 + \kappa)}{2} y^2 + \mathcal{O}(y\log y), \;\; y \to \infty. \tag{3.8b}$$

In both cases, the quadratic far field behaviour results from a balance between the second derivative term and the forcing term. In the far field, the expansion generated is

$$\begin{aligned} u &\sim -1 + \varepsilon[v_0 + \varepsilon v_1 + \varepsilon^{3/2} v_2 + \cdots] \\ &\sim -1 + \varepsilon\left[\alpha y - \varepsilon\frac{\alpha\dot{\rho}_0}{2} y^2 - \varepsilon^{3/2}\frac{\alpha(\dot{\rho}_1 + \kappa)}{2} y^2 + \cdots\right], \quad y \to \infty. \end{aligned} \tag{3.9}$$

As with the 1D analysis, the presence of an intermediate layer is indicated by the fact that the expansion is no longer asymptotic when written in terms of the outer variable y defined in (3.3). This happens when $y = \mathcal{O}(\varepsilon^{-1})$, at which point one needs to introduce the intermediate variables

$$z = \frac{\rho(\tau, s; \varepsilon)}{\varepsilon^{1/2}}, \quad u = w(z, s, \tau; \varepsilon), \quad t = \varepsilon^{1/2}\tau. \tag{3.10}$$

The governing equation (3.2) then becomes

$$-\dot{\rho} w_z = w_{zz} + \varepsilon^{1/2}\kappa w_z + \mathcal{O}(\varepsilon), \tag{3.11}$$

while the local behaviour described in (3.9) indicates that

$$w = -1 + \alpha z - \frac{\alpha\dot{\rho}_0}{2}z^2 - \varepsilon^{1/2}\frac{\alpha(\dot{\rho}_1 + \kappa)}{2}z^2 + \mathcal{O}(\varepsilon). \tag{3.12}$$

In conjunction with the expansion (3.6) for $\dot{\rho}$, we now expand (3.11) with

$$\dot{\rho} = \dot{\rho}_0 + \varepsilon^{1/2}\dot{\rho}_1 + o(\varepsilon^{1/2}), \quad w = w_0 + \varepsilon^{1/2}w_1 + o(\varepsilon^{1/2}), \tag{3.13}$$

and arrive at equations for w_0 and w_1:

$$\begin{aligned}
&w_{0zz} + \dot{\rho}_0 w_{0z} = 0, \ \ z > 0; \quad w_0 = -1 + \alpha z + \mathcal{O}(z^2), \ \ z \to 0^+; \\
&w_{1zz} + \dot{\rho}_0 w_{1z} = -w_{0z}(\kappa + \dot{\rho}_1), \quad z > 0; \quad w_1 = -\frac{\alpha(\dot{\rho}_1 + \kappa)}{2}z^2 + \mathcal{O}(z^3), \ \ z \to 0^+.
\end{aligned}$$

The specified local behaviour as $z \to 0^+$ has arisen from condition (3.12). The explicit solution of this system is

$$w_0 = -1 + \frac{\alpha}{\dot{\rho}_0}(1 - \mathrm{e}^{-z\dot{\rho}_0}), \quad w_1 = \alpha(\dot{\rho}_1 + \kappa)\left[\frac{z\,\mathrm{e}^{-z\dot{\rho}_0}}{\dot{\rho}_0} - \frac{1}{\dot{\rho}_0^2}\left(1 - \mathrm{e}^{-z\dot{\rho}_0}\right)\right]. \tag{3.14}$$

In the limit as $z \to \infty$, and under the assumption that $\dot{\rho}_0 > 0$, we have that

$$u(x_c) = w = -1 + \frac{\alpha}{\dot{\rho}_0} - \varepsilon^{1/2}\frac{\alpha(\dot{\rho}_1 + \kappa)}{\dot{\rho}_0^2} + o(\varepsilon^{1/2}). \tag{3.15}$$

Solving (3.15) asymptotically gives $\dot{\rho}_1 = -\kappa$ and so in terms of the original time variable $t = \varepsilon^{1/2}\tau$, the interface motion is predicted to obey the geometric motion

$$\rho_t = \frac{\alpha}{\varepsilon^{1/2}(1 + u_0(x_c))} - \kappa + o(1). \tag{3.16}$$

3.2 *Bi-Laplacian case*

The fourth-order case proceeds along similar lines and for brevity only partial details are given, along with the final interface motion law. The boundary layer scalings corresponding to Fig. 10 are given by

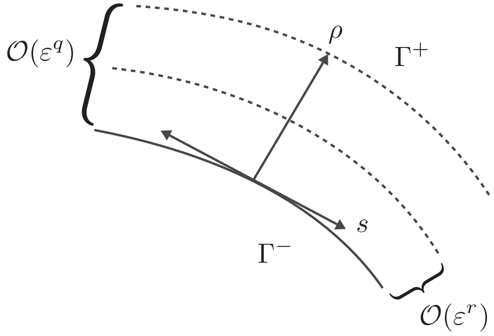

FIG. 10. Boundary Layer structure in the arc-length tangent coordinate system (3.1).

$r = \frac{3}{2}$, $q = \frac{1}{4}$. In the region centred on the interface, we seek a solution in variables

$$u = -1 + \varepsilon v(y, s, t), \quad y = \frac{\rho(x, \tau, s)}{\varepsilon^{3/4}}, \quad \tau = \frac{t}{\varepsilon^{3/4}}, \tag{3.17}$$

in which $\Delta^2 u$ becomes $\varepsilon^{-2}(v_{yyyy} - 2\kappa\varepsilon^{3/4} v_{yyy} + \mathcal{O}(\varepsilon^{3/2}))$. Substituting into (1.1b), the equation for v satisfies

$$-v_{yyyy} + 2\kappa\varepsilon^{3/4} v_{yyy} - \lambda\left[\frac{1}{v^2} - \frac{1}{v^m}\right] = \mathcal{O}(\varepsilon^{3/2}), \quad -\infty < y < \infty. \tag{3.18}$$

Seeking an expansion $v \sim v_0 + \varepsilon^{3/4} v_1 + \cdots$ yields equations for v_0 and v_1

$$-v_{0yyyy} = \frac{\lambda}{v_0^2} - \frac{\lambda}{v_0^m}, \quad -\infty < y < \infty; \tag{3.19a}$$

$$v_0 = 1 + \mathcal{O}(\mathrm{e}^{(\lambda(m-2))^{1/4} y}), \;\; y \to -\infty; \quad v_0 = \alpha y^2 + \xi y + \frac{\lambda}{6\alpha^2}\log y + \mathcal{O}(1), \;\; y \to \infty, \tag{3.19b}$$

$$-v_{1yyyy} + \left[\frac{2\lambda}{v_0^3} - \frac{m\lambda}{v_0^{m+1}}\right] v_1 = -2\kappa v_{0yyy}, \quad -\infty < y < \infty; \tag{3.19c}$$

$$v_1 = \mathcal{O}(y^4\,\mathrm{e}^{(\lambda(m-2))^{1/4} y}), \;\; y \to -\infty, \quad v_1 = c_1 y^3 + c_2 y \log y + \mathcal{O}(y), \;\; y \to \infty, \tag{3.19d}$$

where $\alpha = \sqrt{\lambda(m-2)/(2(m-1))}$ is the constant previously obtained in the 1D case (2.29). In the far field behaviour (3.19d), equations can be formulated for the constants $c_1, c_2, \ldots$; however, the system is not closed until supplemented by an additional condition from matching to an intermediate layer. In this intermediate layer, the variables

$$u(x, t) = w(z, s, t), \quad z = \frac{\rho(x, \tau, s)}{\varepsilon^{1/4}}, \quad \tau = \frac{t}{\varepsilon^{3/4}}, \tag{3.20}$$

are employed which, coupled with the far field behaviours of (3.19), results in the following system for $w(z)$ accurate to $\mathcal{O}(\varepsilon^{1/2})$,

$$w_{zzzz} + \dot{\rho} w_z - 2\kappa \varepsilon^{1/4} w_{zzz} = \mathcal{O}(\varepsilon^{1/2}), \quad 0 < z < \infty; \tag{3.21a}$$

$$w = -1 + \alpha z^2 + \varepsilon^{1/4}(c_1 z^3 + \cdots) + \mathcal{O}(\varepsilon^{1/2}), \quad z \to 0^+. \tag{3.21b}$$

Seeking an expansion of (3.21) with

$$w \sim w_0 + \varepsilon^{1/4} w_1 + \cdots, \qquad \dot{\rho} \sim \dot{\rho}_0 + \varepsilon^{1/4} \dot{\rho}_1 + \cdots \tag{3.22}$$

yields the system of equations

$$w_{0zzzz} + \dot{\rho}_0 w_{0z} = 0, \quad 0 < z < \infty; \tag{3.23a}$$

$$w_0(0) = -1, \quad w_{0z}(0) = 0, \quad w_{0zz}(0) = 2\alpha, \tag{3.23b}$$

$$w_{1zzzz} + \dot{\rho}_0 w_{1z} = 2\kappa w_{0zzz} - \dot{\rho}_1 w_{0z}, \quad 0 < z < \infty; \tag{3.23c}$$

$$w_1(0) = 0, \quad w_{1z}(0) = 0, \quad w_{1zz}(0) = 0. \tag{3.23d}$$

The solution of this system at leading order is given by

$$w_0(z) = -1 + \frac{2\alpha}{r^2}\left[1 - \mathrm{e}^{-rz/2}\left[\cos\frac{\sqrt{3}}{2}rz - \frac{1}{\sqrt{3}}\sin\frac{\sqrt{3}}{2}rz\right]\right], \tag{3.24}$$

where $r = (-\dot{\rho}_0)^{1/3} > 0$ for $\dot{\rho}_0 < 0$. At the following order, a lengthy expression for w_1 can be obtained by solving (3.23c) which ultimately specifies the far field behaviour

$$w(z) = w_0(z) + \varepsilon^{1/4} w_1(z) + \mathcal{O}(\varepsilon^{1/2}) = -1 + \frac{2\alpha}{r^2} - \varepsilon^{1/4}\frac{\alpha}{\sqrt{3}r^4}[\kappa r^2 + \dot{\rho}_1] + \mathcal{O}(\varepsilon^{1/2}), \quad z \to \infty.$$

The matching condition that $u_0(x_c) = u_0(\varGamma = 0) = \lim_{z\to\infty} w(z)$ yields the motion $\dot{\rho}$ of the interface. In terms of the original timescale $t = \varepsilon^{3/4}\tau$, we have that

$$\rho_t \sim \left[\frac{2\alpha}{\varepsilon^{1/2}(1+u_0)}\right]^{3/2} - \frac{2\alpha}{\varepsilon^{1/2}(1+u_0)}\kappa + \cdots. \tag{3.25}$$

In the following section, the validity of this reduced asymptotic description is investigated on several test cases.

3.3 *Numerical examples*

In this section, we compare the above predictions against numerical simulations of the full models (1.1a) and (1.1b). We start with a brief introduction to the method of level sets and then turn to two specific examples.

3.3.1 *Description of level set methods.* To simulate the geometric descriptions for the contact interfaces (3.16) and (3.25), a simple modification of the level-set method described in Smereka (2003) is implemented. In such algorithms for simulating geometric motion, the curve of interest $\varGamma$ is embedded in the zero level set of an associated function ϕ, i.e. $\Gamma = \{(x, y) \in \Omega \mid \phi(x, y, t) = 0\}$. Implicit differentiation of $\phi(x, y, t) = 0$ with respect to t gives rise to the level set equation $\phi_t + \rho_t |\nabla\phi| = 0$, where ρ_t is the normal velocity of Γ. For the interface motion described by ρ_t given in (3.31) and (3.25), we are led to equations of the form

$$\phi_t + (\gamma_1(t) + \gamma_2(t)\kappa)|\nabla\phi| = 0, \tag{3.26}$$

for which we seek a stable and efficient discretization based on finite difference approximations. As discussed in Smereka (2003), stability issues arising from the stiff nature of equation (3.26) can be alleviated by isolating the dominant linear term with the identity $\kappa|\nabla\phi| = \Delta\phi - N(\phi)$, where

$$N(\phi) = \frac{\phi_x^2\phi_{xx} + 2\phi_x\phi_y\phi_{xy} + \phi_y^2\phi_{yy}}{\phi_x^2 + \phi_y^2}. \tag{3.27}$$

This is followed by implicit integration of the linear term and explicit treatment of the remainder, yielding the integration scheme

$$[1 + \delta t\gamma_2(t_n + \delta t)\Delta]\phi_{n+1} = [\phi_n + \delta t\gamma_2(t_n)N(\phi_n) - \delta t\gamma_1(t_n)|\nabla\phi_n|], \tag{3.28}$$

over the time interval $[t_n, t_n + \delta t]$. Calculations are performed on a uniform cartesian mesh with 128 gridpoints in each direction and differential terms are discretized by the standard centred difference formulae. The discretized linear system (3.28) is then inverted by means of an FFT.

3.3.2 *Example* 1: *Laplacian case.* In this example, we demonstrate the predictive qualities of the asymptotic description (3.16) for touchdown region dynamics by considering the evolution of the 'star' shaped initial interface

$$(x, y) = r(\theta)(\cos\theta, \sin\theta), \quad r(\theta) = \sqrt{0.1}(1 + \cos 5\theta). \tag{3.29}$$

An initial condition for the full numerical simulations of (3.16) which has a sharp transition layer around this curve is given by $u(x, y) = a[\tanh[b(x^2 + y^2 - r(\arctan(y/x)^2))] - 1]$ for appropriate values of a, b. As with the 1D example, an expression for the outer solution $u_0(x_c)$ is required in the formulation of (3.16). This is readily obtained by choosing λ large enough so that u_0 is essentially uniform in Ω, except for in a boundary layer near $\partial\Omega$, and satisfies

$$\frac{\mathrm{d}u_0}{\mathrm{d}t} = -\frac{\lambda}{(1 + u_0)^2}, \quad u_0(0) = 0; \implies u_0 = -1 + (1 - 3\lambda t)^{1/3}. \tag{3.30}$$

For the case $m = 4$, this therefore leads us to consider the geometric evolution

$$\rho_t = \gamma_1(t) - \kappa, \quad \gamma_1(t) = \sqrt{\frac{4\lambda}{3\varepsilon}}\frac{1}{(1 - 3\lambda t)^{1/3}}. \tag{3.31}$$

As can be seen from the numerical simulations of Fig. 11, the above equations capture the interface position relatively well. As time increases, the approximation (dashed curve) is first ahead of and then behind the numerically estimated interface (solid curve), the transition approximately occurring at $t = 0.0181$. We believe this is due to the short transient period occurring between the initialization of the

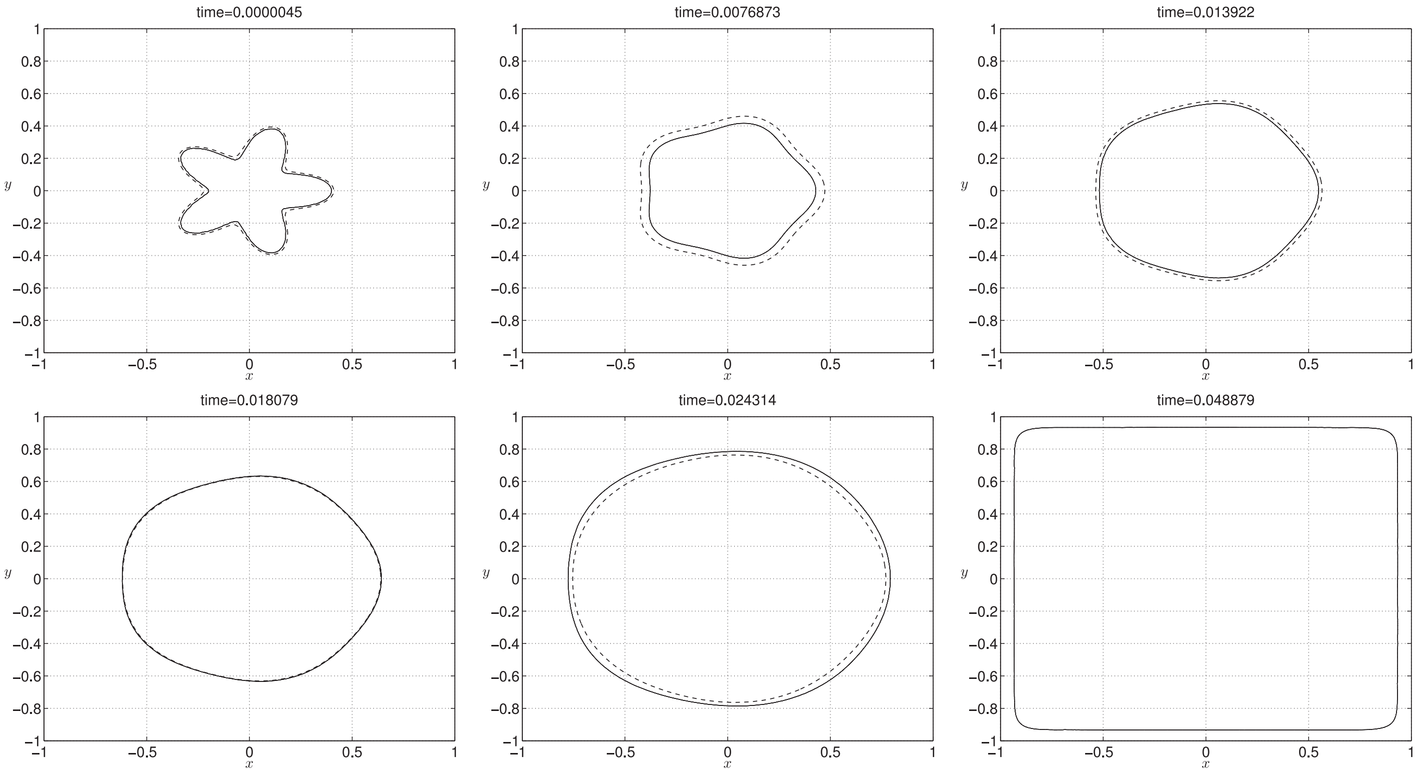

FIG. 11. Evolution of touchdown interface with initial profile (3.29) under parameter values $\lambda = 10$ and $\varepsilon = 0.05$. The solid curve represents the interface calculated from simulations of the full PDE (1.1a) with $m = 4$ on the square region $\Omega = [-1, 1]^2$, while the dashed curves represent the prediction of the reduced asymptotic description (3.31). The final panel displays only the equilibrium interface from the full numerical simulations.

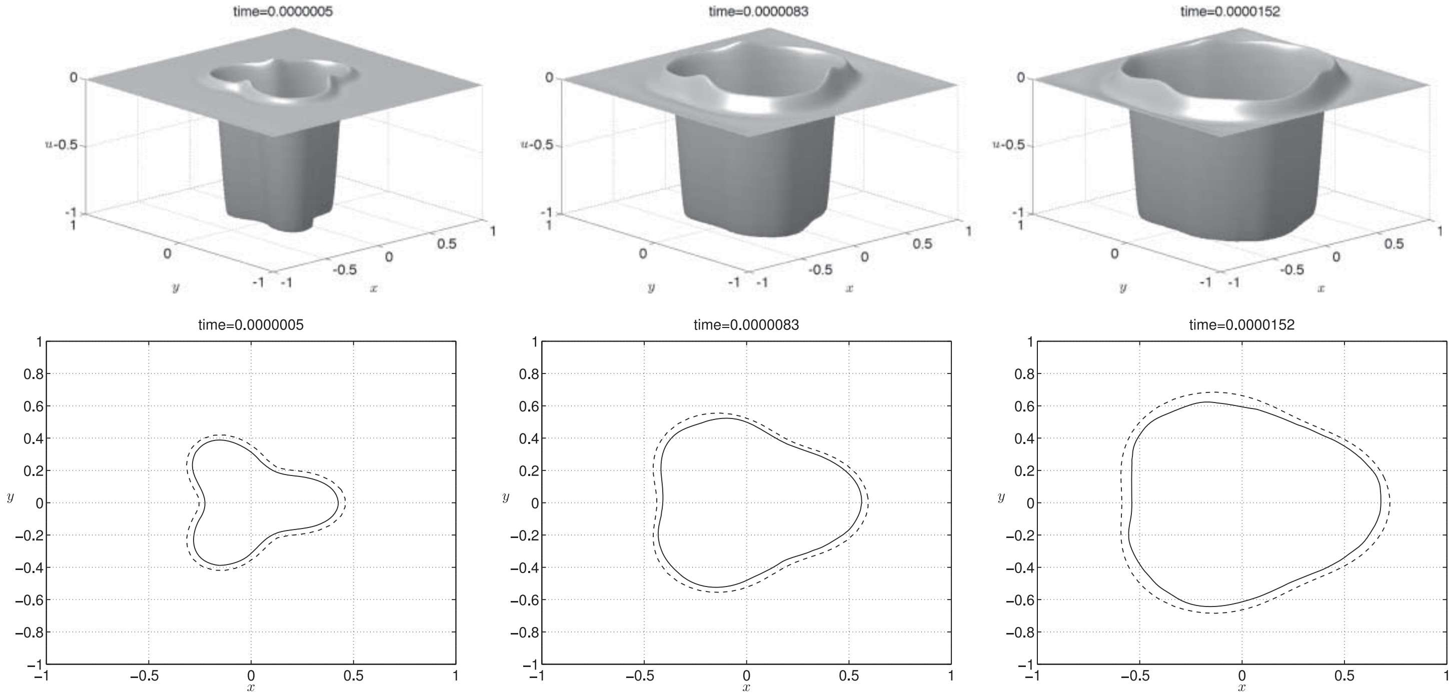

FIG. 12. Evolution of contact interface with initial profile (3.32) under parameter values $\lambda = 2000$ and $\varepsilon = 0.005$. In the lower three panels, the solid curve represents the interface calculated from simulations of the full PDE (1.1b) with $m = 4$ on the square region $\Omega = [-1, 1]^2$, while the dashed curves represent the prediction of the reduced asymptotic description (3.33). The upper three panels show the full solution $u = u(x, y, t)$ at the corresponding time points.

full simulation and settling down into the asymptotic regime. In this transient period, the asymptotic solution (3.31) gets a slight ‘head-start’, which is later equalized.

3.3.3 *Example* 2: *Bi-Laplacian case.* In this example, we use the initial curve

$$(x,y)=r(\theta)(\cos\theta,\sin\theta),\qquad r(\theta)=0.125(1+0.3\cos 3\theta), \tag{3.32}$$

to investigate the validity of the geometric motion (3.25) of the contact interface for the fourth-order problem (1.1b). The ‘shelf-like’ outer solution $u_0=-1+(1-3\lambda t)^{1/3}$ from (3.30) is again applied together with the parameter $m=4$, which reduces (3.25) to

$$\rho_t \sim \left[\frac{2\alpha}{\varepsilon^{1/2}(1-3\lambda t)^{1/3}}\right]^{3/2} - \frac{2\alpha}{\varepsilon^{1/2}(1-3\lambda t)^{1/3}}\kappa + \cdots\,; \qquad \alpha=\sqrt{\frac{\lambda}{3}}. \tag{3.33}$$

Figure 12 displays a comparison between the evolution of the initial curve (3.32) as predicted by (3.33) for the parameter values $\lambda=2000$ and $\varepsilon=0.005$. In this case, the approximation (dashed curve) remains ahead of the numerical interface. We remark that, in this example, the intermediate layer is of width $\varepsilon^{1/4}\approx 0.2659$ and so the layer interacts with the boundary relatively shortly after initialization. In the last time point of Fig. 12, the interface has progressed through half of the domain, while the intermediate layer has already reached the boundary and has begun decelerating. To achieve a good comparison over a larger spatial extent, a smaller ε value would be desirable; however, simulating such values brings numerical challenges due to the stiffness of the regularizing term in (1.1b).

A significant qualitative difference between the second- and fourth-order models (1.1) is the oscillatory nature of the propagating interface. These oscillations are predicted by the analytical formula for the solution in the intermediate layer (3.24) and are evident in the numerical simulations of Fig. 12. This corresponds to the lack of positivity exhibited by fourth-order problems in general, that is initial data of a single sign will not necessarily generate a solution with a single sign for positive time, in contrast to second-order problems.

The amplitude of the overshoot in the interface varies along the interface according to its local curvature. This phenomenon is captured by the correction term $w_1(z)$ determined by equation (3.25).

4. Conclusions

This article is devoted to an analysis of the dynamical properties of the regularized models (1.1a) and (1.1b) that were derived in Lindsay *et al.* (2014). These models describe the dynamics of a microelectromechanical capacitor, as its top plate deflects towards its bottom plate under the effect of an external electric field. They also capture the post-touchdown dynamics of the system, which take place when the top deflecting membrane is in contact with the insulating layer that covers the bottom plate. The region where contact occurs spreads as a function of time until it arrives within a short distance of the boundary, at which point its dynamics is arrested.

In Lindsay *et al.* (2014), we described the resulting equilibrium configurations in great detail, for 1D systems in the limit where the thickness of the small insulating layer (as measured by the parameter ε) goes to zero. Here, we consider both 1D and 2D versions of the models, also in the limit as $\varepsilon\to 0$. In one space dimension, we obtain asymptotic expansions for the speed of the contact point away and near the boundary of the system, and show that the dynamical system describing the moving interface in the vicinity of the boundary admits equilibrium solutions that exactly match the static solutions found in

Lindsay *et al.* (2014). We also compare our predictions for the dynamics away from the boundary to numerical simulations, and show very good agreement between the two. In two space dimensions, we restrict our attention to the dynamics away from the boundary and test our predictions against numerical simulations. The agreement is very good, although not as strong as in the 1D case. This is to be expected since fewer terms are included in the asymptotic expansion for the speed of the moving interface in this case.

The main result of the work presented here is an expression for the speed of the interface delimiting the region where the top plate is in contact with the bottom insulating layer of the capacitor. This speed depends on the local behaviour of the solution near the interface and on the leading-order behaviour of the outer solution evaluated at the contact point. Even though our simulations were performed with symmetric solutions, our formulas for $\mathrm{d}x_c/\mathrm{d}t$ are local and therefore do not rely on any global properties of the solution. In the Laplacian case, the interface velocity is approximated to order $\varepsilon^{1/2}$ in (2.12) for the 1D problem, and to leading order in (3.16) for the 2D problem. In two dimensions, the interface propagates outwards at a speed equal to the speed of the 1D problem corrected by a curvature term. Similar results are obtained at leading order for the bi-Laplacian case, in equations (2.33) and (3.25), respectively. The multiscale nature of the propagating interface, illustrated in Fig. 5, makes the asymptotic analysis particularly intricate. As previously mentioned, in all situations, the interfacial speed depends on the unknown value of the leading-order outer solution u_0 at the contact point $x_c(t)$. In the numerical examples discussed in this article, initial conditions were chosen to ensure that the solution profile was locally flat in the outer region, so that $u_0(x_c)$ remained close to the solution of the associated space-independent problem. This allowed us to illustrate the validity of the asymptotic expansions without having to rely on a numerical estimation of $u_0(x_c)$. A thorough numerical investigation of more general solution profiles could be performed and compared with the analysis presented here, but is beyond the scope of this article.

Regarding potential extensions to this work, there has been recent attention on MEMS models which do not apply the small aspect ratio limit and study the resulting free boundary problem for the deflection $u(x,t)$ (Kohlmann, 2013; Laurençot & Walker, 2013, 2014a,b). It would therefore be very interesting to study the dynamics and potential equilibrium states which arise from effects of regularizations in these systems. From the point of view of the stability of codimension-1 fronts, we note that a somewhat surprising outcome of the numerical simulations of Section 3 is that the 2D interface appears to be stable to transverse perturbations. This contrasts with the instability of the touchdown curves observed in non-regularized 2D models, as, for instance, described in Lindsay *et al.* (2013). It is not clear at present whether the lack of observed instability is genuine, or due to the fact that the interface quickly reaches the boundary in the present simulations. Addressing this question is a difficult problem and a topic for further investigation.

Acknowledgements

We thank F.J. Sayas for assistance with 2D numerical simulations of (1.1b).

REFERENCES

BATRA, R. C., PORFIRI, M. & SPINELLO, D. (2007) Review of modeling electrostatically actuated microelectromechanical systems. *Smart Mater. Struct.*, **16**, R23–R31.

BATRA, R. C., PORFIRI, M. & SPINELLO, D. (2008) Effects of van der Waals force and thermal stresses on pull-in instability of clamped rectangular microplates. *Sensors*, **8**, 1048–1069.

Brubaker, N. D. & Lindsay, A. E. (2013) The onset of multi-valued solutions of a prescribed mean curvature equation with singular nonlinearity. *European J. Appl. Math.*, **25**, 631–656.

Brubaker, N. D. & Pelesko, J. A. (2011) Non-linear effects on canonical MEMS models. *European J. Appl. Math.*, **22**, 455–470.

Fife, P. (1988) *Dynamics of Internal Layers and Diffusive Interfaces*. SIAM Conference Series in Applied Mathematics. http://epubs.siam.org/doi/book/10.1137/1.9781611970180.

Flores, G., Mercado, G., Pelesko, J. & Smyth, N. (2007) Analysis of the dynamics and touchdown in a model of electrostatic MEMS. *SIAM J. Appl. Math.*, **67**, 434–446.

Glasner, K. B. (2003) Spreading of droplets under the influence of intermolecular forces. *Phys. Fluids*, **15**, 1837.

Glasner, K. B. & Witelski, T. P. (2003) Coarsening dynamics of dewetting films. *Phys. Rev. E*, **67**, 016302.

Guo, Y. (2010) Dynamical solutions of singular wave equations modeling electrostatic MEMS. *SIAM J. Appl. Dyn. Syst.*, **9**, 1135–1163.

Guo, Y., Pan, Z. & Ward, M. J. (2005) Touchdown and pull-in voltage behaviour of a MEMS device with varying dielectric properties. *SIAM J. Appl. Math.*, **66**, 309–338.

Guo, Z. & Wei, J. (2008) Infinitely many turning points for an elliptic problem with a singular nonlinearity. *J. London Math. Soc.*, **78**, 21–35.

Guo, Z. & Wei, J. (2009) On a fourth-order nonlinear elliptic equation with negative exponent. *SIAM J. Math. Anal.*, **40**, 2034–2054.

Guo, J.-G. & Zhao, Y.-P. (2004) Influence of van der Waals and Casimir forces on electrostatic torsional actuators. *J. Microelectromech. Syst.*, **13**, 1027–1035.

Huang, W. & Russell, R. D. (1996) A moving collocation method for solving time dependent partial differential equations. *Appl. Numer. Math.*, **20**, 101–116.

Kavallaris, N. I., Lacey, A. A., Nikolopoulos, C. V. & Tzanetis, D. E. (2011) A hyperbolic non-local problem modelling MEMS technology. *Rocky Mt. J. Math.*, **41**, 349–630.

Kohlmann, M. (2013) A new model for electrostatic MEMS with two free boundaries. *J. Math. Anal. Appl.*, **408**, 513–524.

Krylov, S., Ilic, B. R. & Lulinsky, S. (2011) Bistability of curved microbeams actuated by fringing electrostatic fields. *Nonlinear Dyn.*, **66**, 403–426.

Krylov, S., Ilic, B. R., Schreiber, D., Seretensky, S. & Craighead, H. (2008) The pull-in behavior of electrostatically actuated bistable microstructures. *J. Micromech. Microeng.*, **18**, 055026.

Lai, B. (2015) On the partial differential equations of electrostatic MEMS devices with effects of Casimir force. *Ann. Henri Poincare*, **16**, 239–253.

Laurençot, Ph. & Walker, C. (2013) A stationary free boundary problem modelling electrostatic MEMS. *Arch. Ration. Mech. Anal.*, **207**, 139–158.

Laurençot, Ph. & Walker, C. (2014a) A fourth-order model for MEMS with clamped boundary conditions. *Proc. London Math. Soc.*, **109**, 1435–1464.

Laurençot, Ph. & Walker, C. (2014b) A free boundary problem modeling electrostatic MEMS: II. Nonlinear bending effects. *Math. Models Methods Appl. Sci.*, **24**, 2549–2568.

Lin, F. H. & Yang, Y. (2007) Nonlinear non-local elliptic equation modeling electrostatic actuation. *Proc. Roy. Soc. A*, **463**, 1323–1337.

Lindsay, A. E. (2014) An asymptotic study of blow up multiplicity in fourth-order parabolic partial differential equations. *DCDS-B*, **19**, 189–215.

Lindsay, A. E. & Glasner, K. B. (2013) The stability and evolution of curved domains arising from one-dimensional localized patterns. *SIAM J. Appl. Dyn. Syst.*, **12**, 650–673.

Lindsay, A. E. & Lega, J. (2012) Multiple quenching solutions of a fourth-order parabolic PDE with a singular nonlinearity modelling a MEMS capacitor. *SIAM J. Appl. Math.*, **72**, 935–958.

Lindsay, A. E., Lega, J. & Glasner, K. B. (2014) Regularized model of post-touchdown configurations in electrostatic MEMS: equilibrium analysis. *Physica D*, **280–281**, 95–108.

Lindsay, A. E., Lega, J. & Sayas, F.-J. (2013) The quenching set of a MEMS capacitor in two-dimensional geometries. *J. Nonlinear Sci.*, **23**, 807–834.

Lindsay, A. E. & Ward, M. J. (2011) Asymptotics of some nonlinear eigenvalue problems for a MEMS capacitor: Part II: Singular asymptotics. *European J. Appl. Math.*, **22**, 83–123.

Pelesko, J. A. (2002) Mathematical modeling of electrostatic MEMS with tailored dielectric properties. *SIAM J. Appl. Math.*, **62**, 888–908.

Pelesko, J. A. & Bernstein, D. H. (2002) *Modeling MEMS and NEMS*. Boca Raton: Chapman Hall and CRC Press.

Russell, R. D., Xu, X. & Williams, J. F. (2007) MovCol4: a high resolution moving collocation method for evolutionary PDEs. *SIAM J. Sci. Comput.*, **29**, 197–220.

Smereka, P. (2003) Semi-implicit level set methods for curvature and surface diffusion motion. *J. Sci. Comput.*, **19**.

Stewartson, K. & Williams, P. G. (1969) Self-induced separation. *Proc. R. Soc. Lond. A*, **312**, 181–206.

Younis, M. I. & Nayfeh, A. H. (2003) A study of the nonlinear response of a resonant microbeam to an electric actuation. *Nonlinear Dynam.*, **31**, 91–117.